Structural and Magnetic Properties of Mn doped ZnO Thin Film Deposited by Pulsed Laser Deposition

Abdulaziz Baras

In Partial Fulfillment of the Requirements

For the Degree of Master of Science in Materials Science and Engineering

King Abdullah University of Science and Technology

Thuwal, Kingdom of Saudi Arabia

July, 3rd 2011

EXAMINATION COMMITTEE APPROVALS FORM

The thesis of Abdulaziz Baras is approved by the examination committee.

Committee Chairperson: Iman Roqan

Committee Member: Udo Schwingenschloegl

Committee Member: Samir Boulfrad

ABSTRACT

Structural and Magnetic Properties of Mn doped ZnO Thin Film Deposited by Pulsed Laser Deposition

Abdulaziz Baras

Diluted magnetic oxide (DMO) research is a growing field of interdisciplinary study like spintronic devices and medical imaging. A definite agreement among researchers concerning the origin of ferromagnetism in DMO has yet to be reached. This thesis presents a study on the structural and magnetic properties of DMO thin films. It attempts to contribute to the understanding of ferromagnetism (FM) origin in DMO.

Pure ZnO and Mn doped ZnO thin films have been deposited by pulsed laser deposition (PLD) using different deposition conditions. This was conducted in order to correlate the change between structural and magnetic properties. Structural properties of the films were characterized using x-ray diffraction (XRD) and scanning electron microscopy (SEM). The superconducting quantum interference device (SQUID) was used to investigate the magnetic properties of these films.

The structural characterizations showed that the quality of pure ZnO and Mn doped ZnO films increased as oxygen pressure (P_O) increased during deposition. All samples were insulators. In Mn doped films, Mn concentration decreased as P_O increased. The Mn doped ZnO samples were deposited at 600˚C and oxygen pressure from 50-500mTorr. All Mn doped films displayed room temperature ferromagnetism (RTFM). However, at 5 K a superparamagnetic (SPM) behavior was

observed in these samples. This result was accounted for by the supposition that there were secondary phase(s) causing the superparamagnetic behavior.

Our findings hope to strengthen existing research on DMO origins and suggest that secondary phases are the core components that suppress the ferromagnetism. Although RTFM and SPM at low temperature has been observed in other systems (e.g., Co doped ZnO), we are the first to reported this behavior in Mn doped ZnO. Future research might extend the characterization and exploration of ferromagnetism in this system.

ACKNOWLEDGEMENTS

I would like to thank my committee chair, Dr. Iman Roqan, for her advice and financial support and my committee members, Drs. Schwingenschloegl and Boulfrad, for their guidance and support throughout the course of this research. Also, I would like to thank Dr. Singaravelu who worked with me in conducting some of the experiments and discussing the results. In addition, I would like to thank Dr. Bantounas for his help in understanding magnetization theories.

My appreciation also goes to my colleagues, Materials Science and Engineering department faculty and staff for making my time at King Abdullah University of Science and Technology (KAUST) a great experience. I also want to extend my gratitude to KAUST core lab research scientists for their help in operating the instruments that I used in my research.

Moreover, my sincere thanks are extended to my parents for their encouragement and to my facebook friends for their concern and support.

Finally, I thank and dedicate this work to his Majesty King Abdullah Bin Abdulaziz Al-Saud, the custodian of the two holy mosques, for his inauguration and endowment of KAUST.

TABLE OF CONTENTS

TABLE OF FIGURES

TABLE of TABLES

Chapter 1 Introduction

Diluted magnetic semiconductors (DMS) such as transitions metals doped ZnO and GaN have attracted several scientists because of their potential application in spintronic devices. However, researchers have recently started arguing strongly on the origin of ferromagnetism in diluted magnetic semiconductors. The predicted growth mechanisms in these materials are still not yet well-established. Spintronic devices are based on electron charges and electron spins whereas conventional electronic devices are based only on electron charge. The advantages of spintronic devices compared to conventional ones are that spintronic devices save energy and store data. Spintronic data storage maintains a remanence (magnetization) after removing the magnetic field[1], whereas integrated circuit (IC) capacitors store data as charge causing information to be lost when the power is switched off. Moreover, Spintronic devices must have the ability of injecting spin to other layers, spin transport, and spin detection [2]. Diluted magnetic oxide (DMO) materials promise potential applications in different fields[1] (for example medical applications such as cancer detection) [3].

DMSs consist of a non-magnetic semiconductor doped with a transition metal (TM) such as Mn, Fe, Co, etc [4]. In the past, GaAs and InAs doped with Mn semiconductors had attracted most of the work [1]. However, these semiconductors showed low Curie temperatures (T_C). In 2001, the first observation of room temperature diluted magnetic oxides was by Matsumoto *et al*. [5]. They observed a ferromagnetic behavior in Co doped TiO_2 with Curie temperature of 400°C. In the

same year, Dietl *et al*. [6] theoretically predicted room temperature ferromagnetism (RTFM) for Mn doped ZnO based on the Zener model of FM [7]. Afterward, magnetic behaviors were experimentally observed in Mn doped ZnO [8-10]. Evolution of ferromagnetism in ZnO based DMS has not only been tuned depending on dopant-type and concentration but also on the synthesis conditions [8]. It is important that ferromagnetic materials are compositionally homogeneous [4] and possess ferromagnetic behavior at temperatures greater than 300K [11]. Non-homogeneous ferromagnetic materials have short order ferromagnetism which limits their application [12]. This provides motivation to find the optimal conditions to grow diluted magnetic oxides (see chapter 4).

The objective of this work is to synthesize ZnO based diluted magnetic oxide thin films. This is conducted in order to investigate the effect of varying the deposition conditions on the evolution of room temperature ferromagnetism (RTFM). This leads to the correlation of the origin of RTFM to crystal structure modification and the identification of plausible defects.

This thesis will consist of 5 chapters. Chapter 1 is the introduction. Chapter 2 will present a background and a brief review in ZnO and Mn doped ZnO including the magnetic theory. Chapter 3 will describe the techniques used in this work and their physical theory. Chapter 4 will report our results of the structural and magnetic properties of Mn doped ZnO thin films including the synthesis methods. Finally, in Chapter 5 a discussion of the results and the derived conclusions are presented.

Chapter 2 ZnO and the Magnetic Properties of Mn doped ZnO

This chapter will present a brief review of the properties of ZnO such as its crystal structure and band structure. Then this chapter will introduce the magnetic theory and the physical mechanisms that have been used to explain the ferromagnetic behavior of DMSs. Finally a brief review in Mn doped ZnO properties will be presented. Practical attention will be given to the magnetic properties of Mn doped ZnO thin films.

2.1 ZnO Crystal Structure

In 1935, the research of Zinc oxide (ZnO) started by Bunn who studied its lattice parameters [13]. ZnO was well-known for its optoelectronic applications. More recently, it has attracted attention due to its low production cost and wide range of properties. For example, it can be grown as a single crystal substrate, and exhibit *p*-type conductivity and ferromagnetic behavior when doped with transition metals (TM) and its low cost production [13]. ZnO has wide applications. It is used in displays, field emission sources, biological and piezoelectric sensors, and light emitters and detectors [13, 14].

ZnO is an inorganic compound stable at room temperature and crystallizes in the wurtzite structure (Figure 1.c) [14]. Also, ZnO can be grown as cubic zincblende structure (Figure 1.b), and rocksalt structure (Figure 1.a) [13]. The zincblende structure is only stable when it is grown on cubic structure substrates; while the rocksalt structure requires a high pressure growth condition [14]. The

ZnO hexagonal lattice belongs to $P6_3mc$ space group [14] and its lattice parameters are a = 0.325nm and c = 0.521nm [15]. ZnO powder is shiny white while its thin films are transparent. This semiconductor has a wide direct band gap (Figure 2) of 3.4eV and a large exciton binding energy of 60mV [15]. This wide band gap enables ZnO to be used in power devices and at high temperature [13].

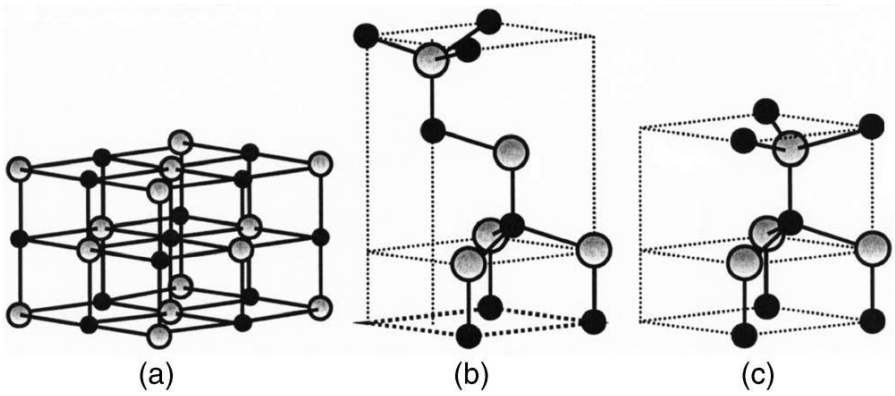

Figure 1: Stick and ball representation of ZnO crystal structures: (a) cubic rocksalt, (b) cubic zincblende and (c) wurtzite. Gray spheres denote Zn and black spheres denote O atoms [13].

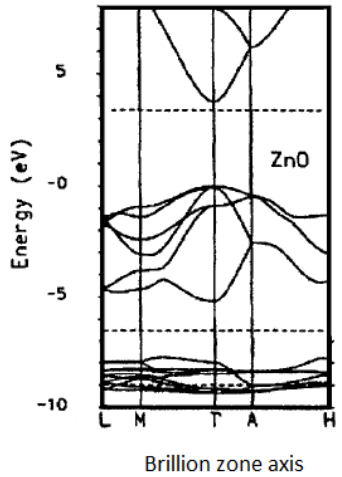

Figure 2: Calculated ZnO band structure using local density approximation with self—interaction corrected pseudopotential approach [13].

2.1.1 Structural Properties of Mn doped ZnO

Shan *et al* deposited pure wurtzite and Mg doped ZnO thin films with different concentration (0.5 – 5 %) using pulse laser deposition (PLD) [16]. They observed that the preferred orientation was (002) which indicate epitaxial c-axis films. In general, the c-axis orientation is the preferred direction with many other deposition methods as well [17]. Therefore, large grains of the films will be formed at this direction. As the ZnO film was doped with Mg, the position of (002) peak shifted to the right from 34.39˚ to 34.55˚ as Mg concentration increased (0.0 – 5%). Bragg's law was used to calculate the lattice constants, which decreased as Mg concentration increased.

$$\frac{1}{d_{hkl}^2} = \frac{4}{3}\left(\frac{h^2 + hk + k^2}{a^2}\right) + \frac{l^2}{c^2} \qquad (1)$$

$$\sin^2\theta = \frac{\lambda}{4}\left(\frac{4}{3}\,\frac{h^2 + hk + k^2}{a^2} + \frac{l^2}{c^2}\right) \qquad (2)$$

For (100) plane $a = \frac{\lambda}{\sqrt{3}\sin\theta}$ and for (002) plane $c = \frac{\lambda}{\sin\theta}$

This indicated that the lattice shrunk as dopant concentration increased. They reported that Mg was positioned at an interstitial site. However, for Mn doped ZnO, Zhang *et al* reported a shift to a lower angle of (002) plane and hence an increase in the c-axis from 0.519 to 0.521nm as Mn dopant concentration increased from 0% to 5% for ZnO thin films deposited by PLD [18]. He suggested that Mn substituted Zn. Venkataraj *et al* reported an MnO_2 phase for the peak at 44.5˚ in doped ZnO films

[11]. Therefore, the dopants affect the quality of the crystal structure of ZnO films which influence the electric, optical and magnetic properties of the materials.

M. Diaconu *et al*. [19] reported ferromagnetic (FM) behavior from Mn doped ZnO grown by PLD at room temperature. SEM indicated the formation of clusters on the surface of the films as shown in Figure 3. These clusters are either MnO or Mn_2O and are anti-ferromagnetic (AFM) at 10K. In addition, ferromagnetism increased as Mn concentration increases. They concluded that the origin of FM is from the impurity band which will be discussed in section 2.4.

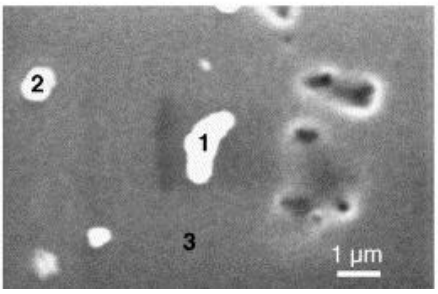

Figure 3: SEM image showing clusters on the surface [19].

S. Karamt *et al*. [20] Reported Mn doped ZnO film with smooth surface. Despite that there were bright areas (Figure 4).They were described as droplet.

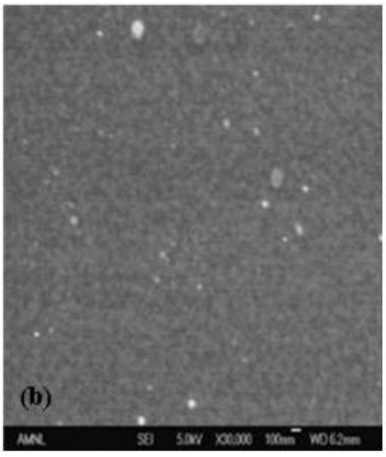

Figure 4: SEM images showing droplet [20].

J. Mera *et al*. [21] reported FM at 300 K for $Zn_{0.9}Mn_{0.1}O$ films. These films were smooth and dense since there were no pores as shown in Figure 5.a. Figure 5.b shows the energy dispersive x-ray spectroscopy (EDS) data which showed there were no foreign elements.

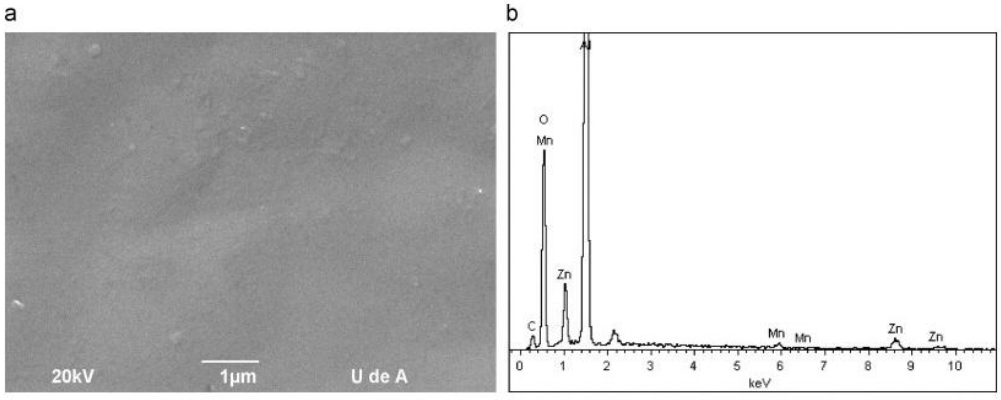

Figure 5: (a) SEM morphology of Mn doped ZnO film showing smooth surface (b) shows the corresponding EDS analysis [21].

SEM images of 1 nm resolution are used to investigate microstructure surface morphology. In addition, other signals (e.g. BSE and EDS) used to study specimen composition and chemical analysis, respectively. The SEM images are used to realize the existence of clusters or defects (e.g. pores) in the surface which may be results in FM in Mn doped ZnO.

2.2 Magnetism

We will introduce in this section a brief summary of the magnetic theory and the magnetic models that have been established to explain the magnetic mechanisms in the DMSs.

2.2.1 Introduction to Magnetism

The magnetic moment (m) is the primary unit in magnetism [22]. The magnetic moment is generated when a current I is flowing in a closed circuit of an area A and is given by equation (3) [23].

$$m = I \, . A \qquad (3)$$

m unit is A.m^2 or Joule per Tesla (JT^{-1}) which comes from $E = -m \cdot B$, where E is the energy of the magnetic moment in Joule (J), and B is the magnetic flux density (induction) and its unit is Tesla (T), 1 Tesla = 10,000 Oerstd (Oe) [22]. Figure 6 shows this relation. Another important unit is Bohr magneton (μ_B) which is the atomic magnetic moment and defined by equation (4) [22].

$$\mu_B = \frac{e\hbar}{2m_e} \qquad (4)$$

Where e is the electron charge = -1.602×10^{-19} C, $\hbar$ = $1.0546\text{x}10^{-34}$Js is Planck constant, m_e is mass of the electron = 9.10938291×10^{-31} Kg.

The magnetic field is described by another important vector called field strength (H) which is related with the magnetic flux induction by equation (5) and (6) in vacuum and solid, respectively [22].

$$B = \mu_0 H \quad (5)$$

$$B = \mu_0 (H + M) \quad (6)$$

$\mu_0 = 4\pi\text{x}10^{-7}$ Hm^{-1} which is the permeability of free space. M is also one of the most important magnetic properties; it is the magnetization which is the magnetic moment per unit volume, area, or gram [22]. Another important characteristic is the susceptibility (χ). It measures the magnetization variation with an applied field [24]. It is a dimensionless unit and given by equation (7).

$$\chi = \frac{M}{H} \quad (7)$$

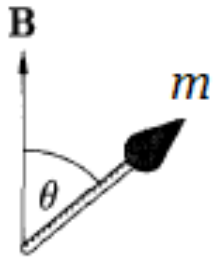

Figure 6: Magnetic moment m in a magnetic field B [22].

2.2.2 Materials classification based on their magnetic behaviors

Different materials exhibit different behaviors in presence of an external magnetic field [23]. These behaviors depend on materials magnetic moments order and interaction [23]. In this section, magnetic behaviors of different materials are presented.

In diamagnetic materials, such as undoped GaN and ZnO), the atoms posse ordered and zero net atomic magnetic moment, and induce opposite magnetic field of the applied field direction. Diamagnetism is a relatively strong effect and almost independence of temperature [23]. Elements with fully filled shells are diamagnetic [23].

In paramagnetic materials (such as Mn), a weak interaction occurs between the magnetic moments of the atoms [23]. These materials have random oriented magnetic moments and almost do not respond to an applied magnetic field. Paramagnetism is a weak effect and affected by temperature [23].

Most of magnetic moments of ferromagnetic materials are aligned to the direction of an applied magnetic field [23]. These materials are strongly affected by temperature; and become paramagnetic material above a specific temperature called the “Curie temperature”. This is because their phonons break the interaction between the aligned moments [23].

There are other two behaviors that are related to the aligned magnetic moments: anti- ferromagnetic and ferrimagnetic [23]. Anti-ferromagnetic (AFM) materials align almost half of their magnetic moments to the magnetic field and the

other half in the opposite direction to the field. Whereas, ferrimagentic materials align small portion of their magnetic moments to the applied magnetic field [23]. Figure 7 shows the difference between ferromagnetic, anti-ferromagnetic and ferrimagnetic materials in a presence of an applied magnetic field.

Table 1 summarizes the magnetic behaviors due to the external applied magnetic field and the susceptibility vs. temperature for some magnetic materials.

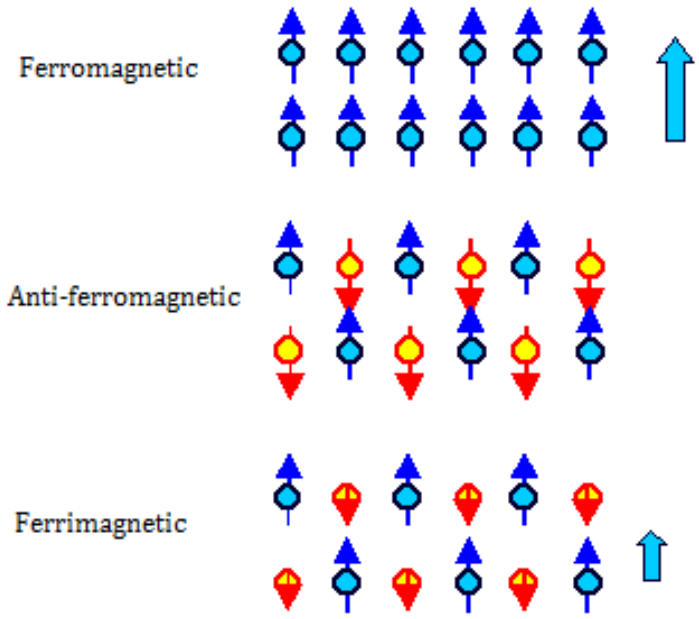

Figure 7: Magnetic moment alignment of ferromagnetic, anti-ferromagnetic and ferrimagnetic materials [23].

Table 1: Shows the magnetic behavior and suscepitibility of diamagnetic, paramagnetic and ferromagnetic materials. The dash lines shows the inverse of suscepitibility [23].

Type	Magnetic behavior	Susceptibility
Diamagnetic	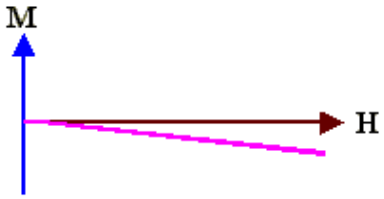	
Paramagnetic	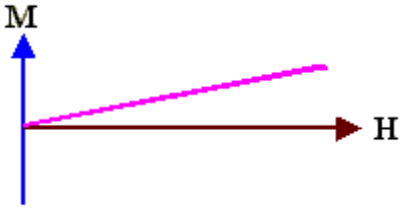	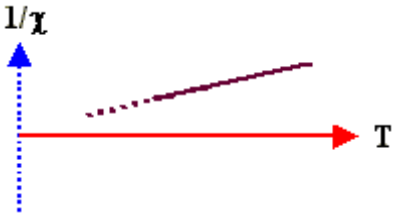
Ferromagnetic	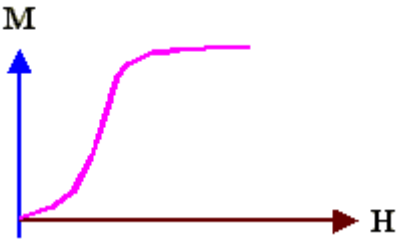	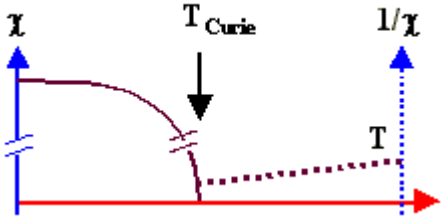

2.2.3 Origin of Ferromagnetism

A. Weiss Theory

In 1906, Pierre Weiss was the first scientist who explained the behavior of ferromagnetism (FM) [24]. His theory called the molecular field theory (MFT) and declared that there are local moments inside a solid which align together with an

applied field [25]. These moments form small regions called magnetic domains which align with the applied field as shown in Figure 8 [24].

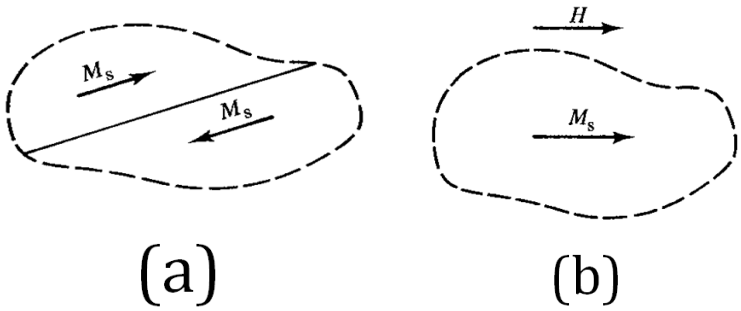

Figure 8: Weiss magnetic domains. (a) Without applied field and (b) with an applied field [24].

B. Heisenberg and Dirac theory

Heisenberg and Dirac developed the MFT and proved that FM is due to coulomb interaction [25]. Coulomb interaction arises a continuous exchange of an electron from one atom to another adjacent atom at high frequency, about 10^{18} times per second in the hydrogen molecule [24]. The energy of this exchange is given by equation (8) [24].

$$U_{ex} = -2J\, S_i\, S_j\, \cos \emptyset \qquad (8)$$

Where U_{ex} *is* the energy of interaction between two atoms, J is the exchange integral, S is the spin momentum and ∅ is the angle between the spins. The exchange integral depends on the ratio r_a/r_d where r_a is the atomic radius and r_d is 3*d* shell radius [24]. Figure 9 shows the exchange integral for some of the transition elements, it is called Bethe-Slater curve [24].

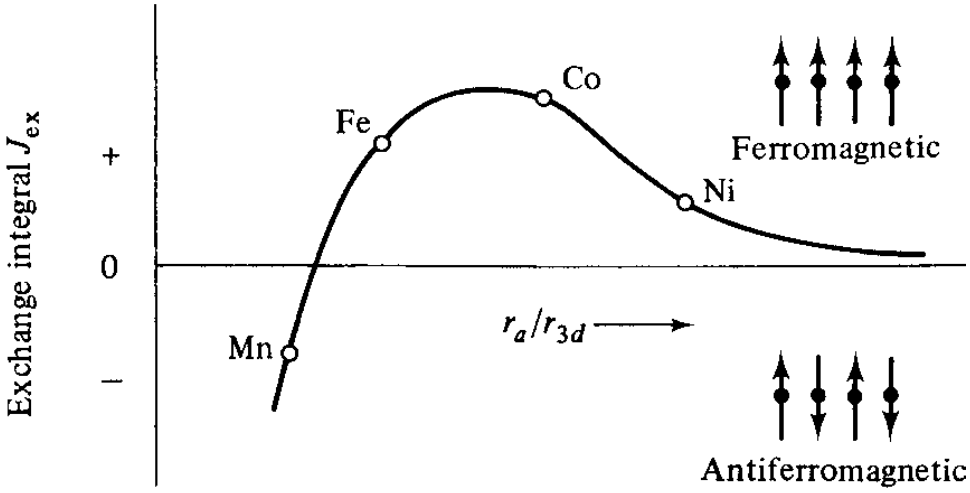

Figure 9: Exchange integral curve [24].

C. Band theory:

The energy levels of a free atom consist from discrete values (states). Table 2 shows the number of electrons that a level can contain [24].

Table 2: Atomic energy levels [24].

Shell	*K*	*L*		*M*			*N*	
Subshell	1*s*	2*s*	2*p*	3*s*	3*p*	3*d*	4*s*	...
Capacity	2	2	6	2	6	10	2	...

The *s* level has one level but two states, one electron spins up and the other spins down as Heisenberg discovered. In addition, when atoms are brought close to each other, each of these levels splits into N levels where N is the number of atoms creating bands of energies, Figure 10 shows the energy bands [24].

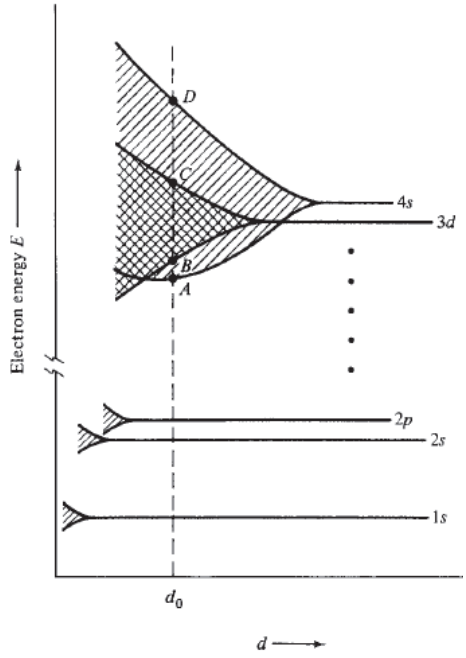

Figure 10: Energy bands [24].

s shells electrons have no role in ferromagnetism [24]. Now, think about one atom which has one electron. When 10 of this atom are brought together, the level will split into 10 states and the 10 electrons will fill the bottom 5 levels with opposite spins (Figure 11.a) [24].

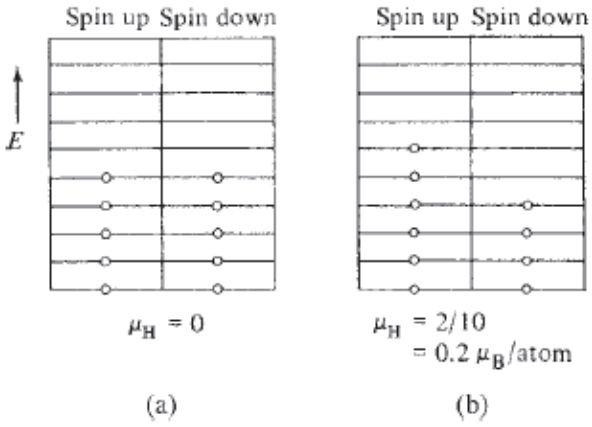

Figure 11: Energy bands with (a) balanced and (b) unbalanced spins [24].

Assume a force change a spin of one of these electrons (Figure 11.b). The difference in total spins = 2/10 =0.2 μ_B/ atom. This force is called the exchange force [24]. A large exchange force is needed when the spaces between the levels are wide (deep) [24].

2.3 Origin of FM in Diluted Magnetic Oxides

There are many models which describe the origin of FM in TM doped oxides. It can be classified into three categories: carrier exchange interaction, defect based model and secondary phases [4].

2.3.1 Indirect Exchange: (RKKY)

It is the coupling between two local magnetic ions through a free carrier (Figure 12) [22]. These carriers align also local moments with them [22].

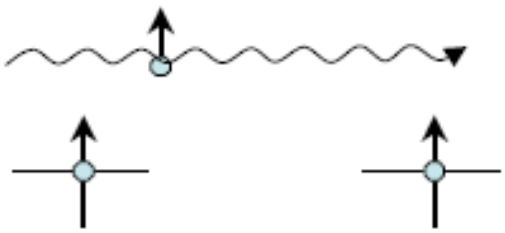

Figure 12: Schematic of RKKY model [26].

2.3.2 Superexchange: (Zener model (indirect coupling))

The free electrons come from metal ions and have spins parallel to the core shells electron spins. The ions are coupled through O^{2-} (Figure 13). If the ions have opposite spin direction (that is AFM), the free electrons will be delocalized, thus

lowering the energy of the system. So, this exchange usually favors AFM. However, if ions of same spin direction are coupled, the system will have high energy because Pauli Exclusion Principle resists adjacent parallel electrons. So, FM is not favored [22].

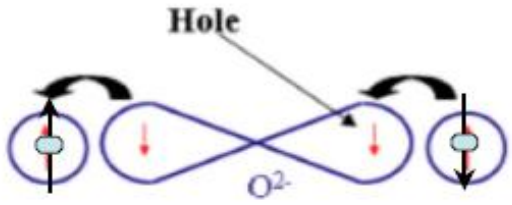

Figure 13: Superexchange model, oxygen mediates the exchange [26].

2.3.3 Direct, Double exchange

The double exchange happen when the dopant has more than one oxidation state like Mn which can be Mn^{3+} or Mn^{4+} [22]. Therefore, in the conduction band of Mn^{3+} has one electron but Mn^{4+} has no free electrons. If Mn^{4+} core shell are parallel with Mn^{3+} (Figure 14) it will be easy for the electron to hop to the other ion and ferromagnetism is induces. These hopper electrons will keep hopping between these ions [22].

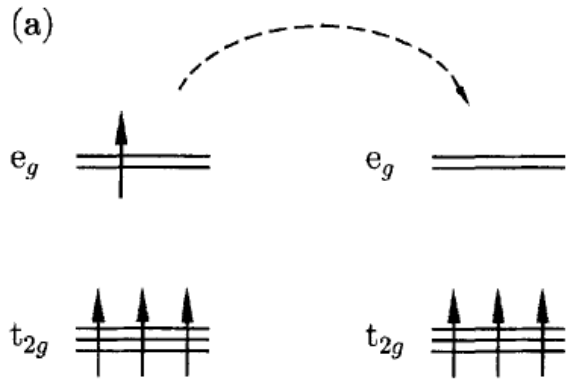

Figure 14: Double exchange FM where the ions have parallel spins [22].

Experimental work shows that carriers are not necessary for RTFM, so the mediated carrier exchange is unable to explain this [4]. Bound magnetic polaron (BMP) model could explain the origin of FM based on the defects. A polaron is an electron confined in a hydrogenic orbital induced by an oxygen vacancy (Vo) (Figure 15) [4]. The size of the polaron depends on the size of the hydrogenic orbital estimated in Co-Zn to be 7.8Å [4]. This polaron couples dopant moments and enhances FM [4]. Dopant acceptor levels will allow the trapped carriers to exchange between the impurity (dopant) atoms [4]. Moreover, if the impurity levels are shallow, FM will be enhanced [4].

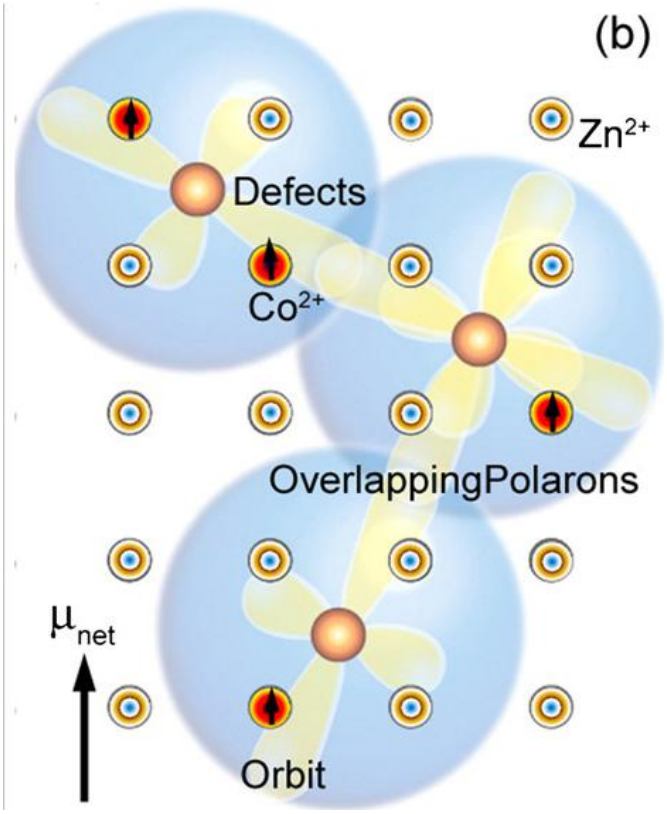

Figure 15: Three polarons (blue circles) [4].

2.4 Mn doped ZnO thin films

In this section, the experimental work of many groups who focused on growing Mn doped ZnO by pulsed laser deposition (PLD) will be presented. Sharma *et al*. reported RT ferromagnetism (RTFM) for Mn (<4 at. %) doped ZnO [12]. They observed ferromagnetism (FM) above 425K for $Zn_{0.978}Mn_{0.022}O$ films grown on fused quartz with magnetization of 0.05 e.m.u./g at 300K (Figure 16). It was ensured that there was no secondary phases nor clusters. Moreover, Mn replaced Zn in the ZnO hexagonal matrix. Their *ab initio* calculation showed that the FM state has a lower energy than that of anti-ferromagnetism (AFM) state which was consistent

with their experimental results. They stated that the results agree with carrier induced FM.

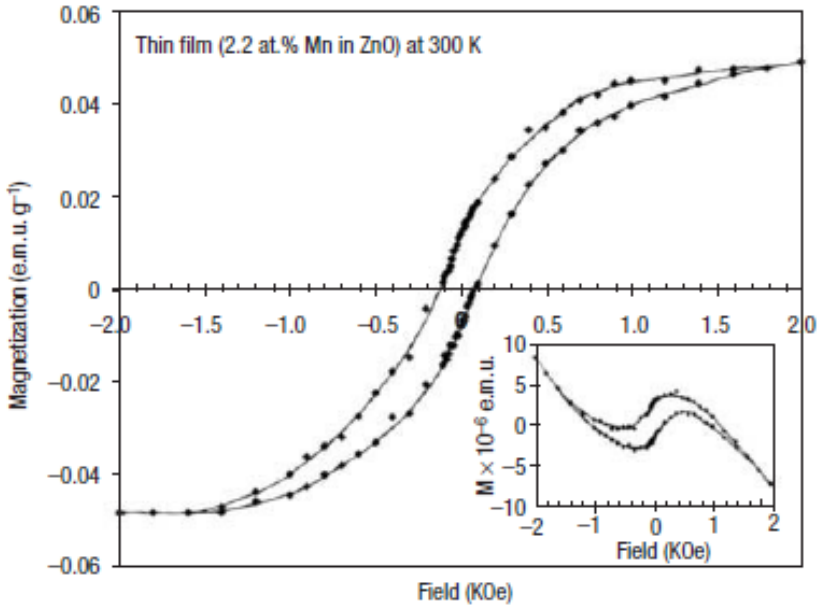

Figure 16: MH loop at 300 K for Mn doped ZnO film after subtracting the diamagnetic contribution of the substrate. The inset shows the row data as taken from SQUID measurement (before subtracting substrate effect) [12].

N. Hong *et al*. [27] observed FM at 300K for $Zn_{0.09}Mn_{0.01}O$ grown on c-sapphire with value of 7emu/cm^3. Pure ZnO films showed also FM at 300K with value of 3.3 emu/cm^3. After annealing these pure films, no change in magnetization was observed. From the different magnetization values of different film thickness, and the different in measurement direction (parallel and perpendicular to the film plane), (Figure 17), it was concluded that magnetism was due to defects and it is anisotropic. These defects were related to Zn sites and not to oxygen vacancies (V_O) since annealing has no effect where annealing reduces V_O presence. This agreed

with the theoretical model of N. Huong *et al*. [28] which stated that there are other origins of FM in ZnO other than V_O. They concluded that Mn did not play any role in the evolution of FM even though it enhanced FM through double exchange interaction. Nevertheless, J. Mera *et al*. [21] reported FM at 300 K for $Zn_{0.9}Mn_{0.1}O$ films grown on c-sapphire substrates with M_S equal to 3 x 10^{-5} emu. It was reported that Vo creates FM from the spins of unpaired electrons, so called bound magnetic polaron and no secondary phases were detected.

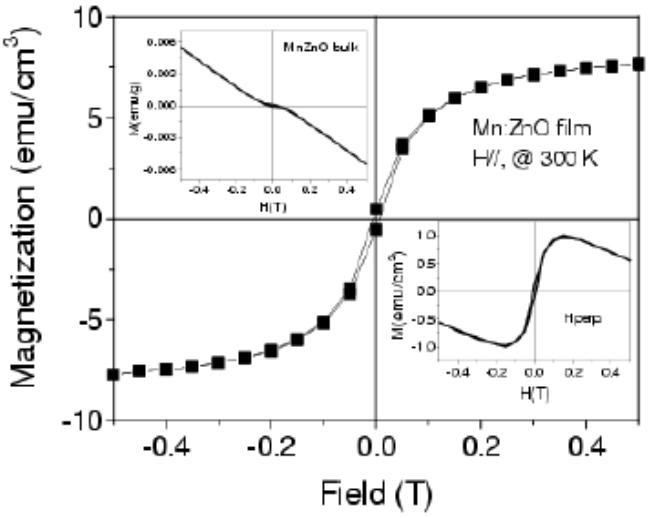

Figure 17: MH loop at 300 K for Mn doped ZnO film in the parallel configuration while the bottom inset shows the MH loop for the same film but in the perpendicular configuration. The upper inset shows the MH loop for the film target (bulk) [27].

The impurity band model is one of the important models that have been used to explain the magnetization mechanism in Mn doped ZnO. M. Diaconu *et al*. [19] reported FM at 300K for $Zn_{1-x}Mn_xO$ films grown on c- sapphire (x= 9.1 and 6.5) with values of 0.035 and 0.003 emu/g whereas $Zn_{0.982}Mn_{0.018}O$ was paramagnetism

(Figure 18). Their results support the impurity band model since the magnetization increased as the number of defects increased. K. Nielsen *et al.*[29] observed FM in $Zn_{0.95}Mn_{0.05}O$ films grown at 200°C with magnetization equal to 0.5 μ_B/Mn ion whereas films grown at 600°C were not ferromagnetic. Impurity bands were observed in 200°C films; therefore, it was concluded that these impurity bands are the origin of FM as Venkatesan *et al.* [30] proposed in their spin split orbit model (Figure 19).

It was believed that P_O is the main factor which affects FM. Di Trolio *et al.*[31] reported FM above 500K for ZnMnO with Mn concentration in the prepared target 4at% and 10at%, the magnetization saturation (M_S) was 0.96 and 0.36 emu/g respectively. There was no specific conclusion on the origin of FM. Although their magnetic values changed with changing deposition P_O, deposition temperature (T_d) and Mn dopant concentration, it was concluded that the origin of FM is either from defects, intrinsic or Mn dopant. They found secondary phases of MnO2, Mn3O4, ZnMn2O4 and ZnMnO3 from the XRD pattern. Although these secondary phases are antiferromagnetic, FM was observed in the compound. K. Jeon *et al*. [32] observed FM at 300K in ZnMnO film prepared from a target of 0.3 mol of Mn grown on c-sapphire with M_S equals to 3emu/cm^3. It was concluded that low P_O creates more vacancies, these vacancies trap charge carriers. Therefore, their low Po samples showed higher resistivity. These trapped carriers with the strong s-d exchange coupling mediate FM between Mn Ions.

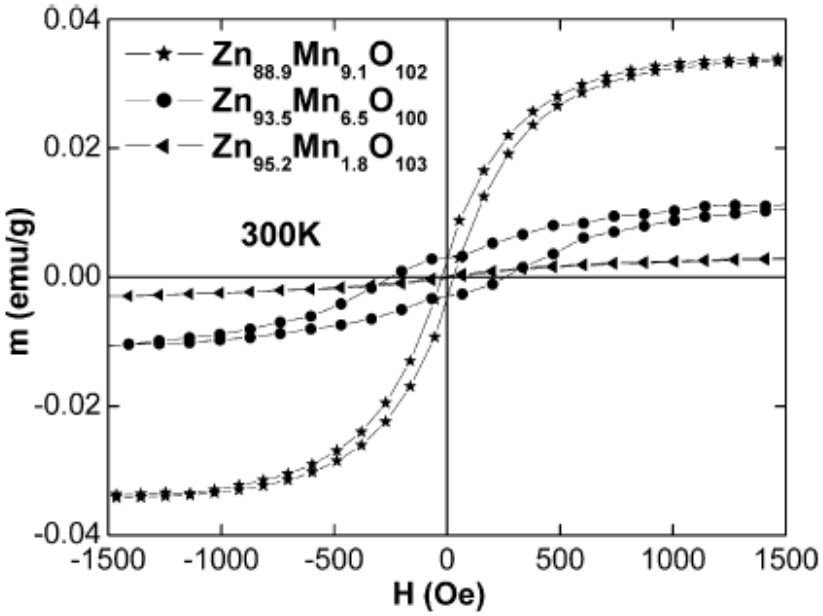

Figure 18: MH loop at 300 K for Mn doped ZnO films with different Mn concentration [19].

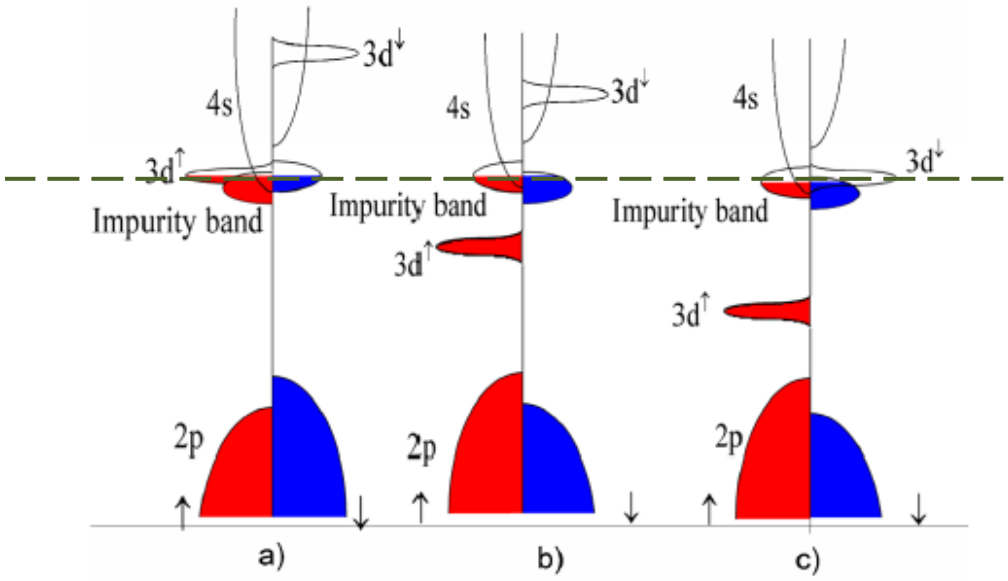

Figure 19: Schematic density of states for (a) Ti, (b) Mn, and (c) Co. The Fermi level lies in a spin-split donor impurity band (the dash line) [30].

However, several researches did not observe an FM behavior from ZnMnO films for several reasons that depend on the deposition conditions. K. Ueda *et al*. [33] did not observe FM in $Zn_{1-x}Mn_xO$ films grown on Al_2O_3 (1120) deposited from $Zn_{1-x}Mn_xO$ target (x= 0.05-0.25). It was concluded that there were not enough carries to mediate FM whereas FM was observed in films with more carriers. T. Fukumura *et al.* [8] reported AFM for $Zn_{0.98}Mn_{0.02}O$ with spin glass behavior. A. Tiwari [10] observed paramagnetism in $Zn_{1-x}Mn_xO$ deposited on c –sapphire.

In summary, different results and observations have been reported on the origin of FM in Mn doped ZnO. This is an attempt to draw a picture and initiate the work in this system.

Chapter 3 Experimental Techniques

In this chapter, the techniques used in characterizing the films are presented. These techniques are XRD, SEM, SQUID and PLD.

3.1 X-Ray Diffraction: theoretical Background

X-ray diffraction (XRD) is a technique where materials structural properties are investigated by measuring the deflection of an x-ray beam from the material. The XRD technique is a nondestructive technique with a detection limit of less than 3% [19]. It is used to identify thin films elements and preferred growth direction, measure lattice parameters and grain sizes, and crystal quality [19]. The XRD setup consists of a beam source, a stage and a detector as shown in Figure 20.

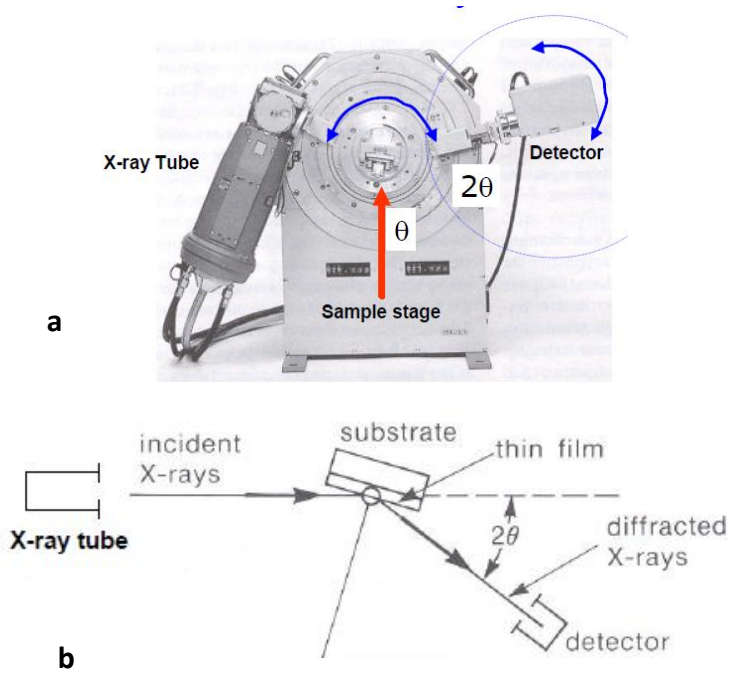

Figure 20: XRD components: source, sample stage and detector.(b) Schematic of XRD path [19].

An x-ray beam is generated when a metal target is stroked with high energy electrons [34]. Pure metal copper is the most common target which generates x –ray of 0.1541nm in wavelength [34]. Thin films are mounted on a rotating stage; this stage could be rotated about two to six axes depending on its design. These rotations have different applications (e. g. material quality and eliminating substrates defects).

X-ray diffraction measurements rely mainly on Bragg's law, equation (9) , which states that:

$$2d \sin\theta = n\lambda \qquad (9)$$

Where d is the spacing between parallel planes, θ is the angle of incident beam, n is an integer number, and λ is the beam wavelength. Constructive interference between incident and reflected beams happens only if Bragg's law is satisfied. λ is known, θ is taken from XRD spectra, and then d is calculated. Figure 21 is a schematic of Bragg's law

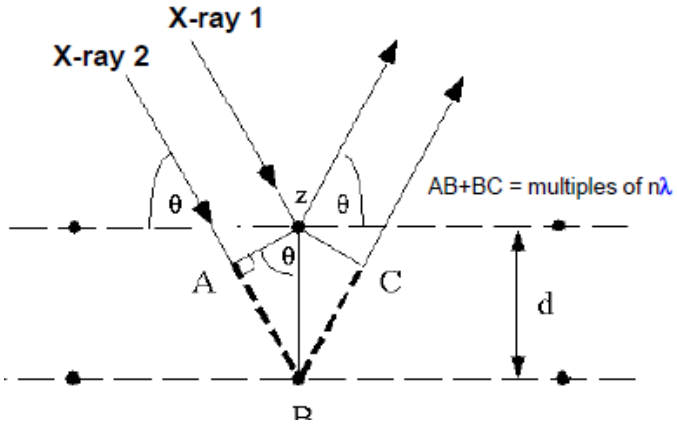

Figure 21: Schematic of Bragg's law [19].

Lattice parameters are derived from another equation which varies according to materials crystal structure (cubic, tetragonal, hexagonal, etc.). For example, equation (10) represents this relation for cubic crystals.

$$d_{hkl} = \frac{a}{\sqrt{(h^2 + k^2 + l^2)}} \quad (10)$$

where *a* is the lattice parameter and *hkl* are the miller indices which represent the crystallographic planes. From equations (9) and (10), *a* can be calculated. Information about peak positions of XRD spectrum for different lattice structures can be found from the International Centre for Diffraction Data [11].

3.2 Scanning Electron Microscope Theory and Background

Earlier, optical microscopes were used to investigate materials morphologies. One of the limitations of these microscopes is their resolution (ΔR) which is defined as the smallest distance between two points in the sample that can be identified in the image [35]. ΔR is found from equation (11)

$$\Delta R = \frac{0.61\,\lambda}{r \sin\theta} \quad (11)$$

λ is light wavelength in nm (for visible light range is 380-750 nm), *r* is the medium refractive index, θ is half of the light cone angle on the specimen. Figure 22 is a schematic diagram explaining equation (11) [35]. Short wavelength is needed to increase the resolution.

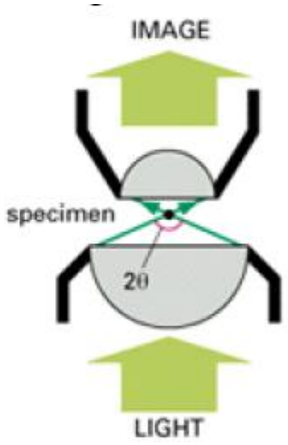

Figure 22: Schematic of resuluation equation [35].

In 1930, the first electron microscope was built by Ruska and Knol [35]. The resolution is now dependent on the electron wavelength. Electron wavelength is shorter than light wavelength by approximately five orders of magnetiude. Electron wavelength can be tuned depending on electron beam accelerating voltage (e.g. 100kV gives 0.0037nm and 1000 gives 0.00087nm) [35]. The evolution of electron microscopes required 3 essential functional devices: beam generating devices, beam focusing devices and signals detecting devices [35]. Figure 23 shows a schematic of an SEM.

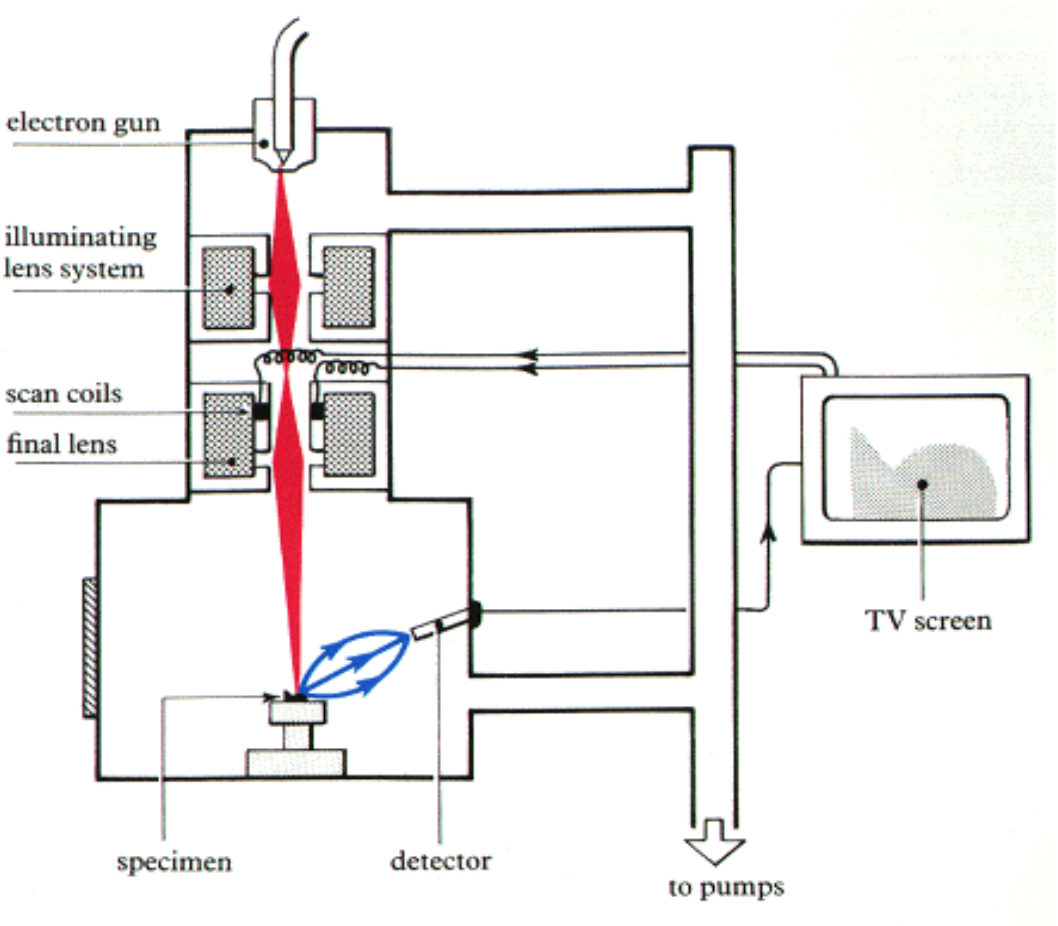

Figure 23: Schematic of SEM design [35].

There are two types of electron beam sources: thermionic source and Schottky gun (called field emission gun). A voltage difference between a cathode an anode is created to accelerate the extracted electrons from the source [36]. Figure 24 shows a schematic of Schottky gun [35]

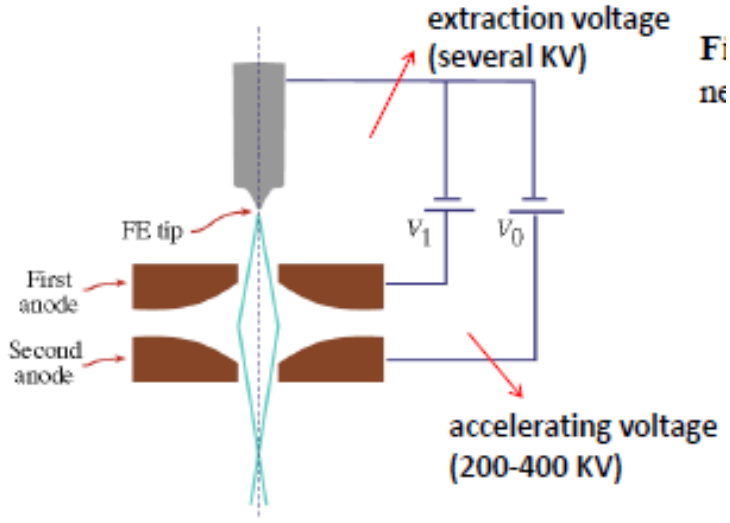

Figure 24: Schematic of Schottky gun [35].

In thermionic source the electron are extracted through thermal vibration which breaks the electrostatic forces that hold the electrons and then electrons are injected [35]. Schottky gun consists of a Tungsten needle of a 100 nm tip [35]. The applied electrical field (E) is enlarged in the tip:

$$E = V/r \qquad (12)$$

Where V is the applied voltage (v) and r is tip radius (nm). As a consequence of the enlarged field, Schottky barrier at the tip decreases. Hence, electrons are freed. The Schottky barrier is the difference between Fermi level and the minima conduction band [37].

Light beam in optical microscopes is focused by glass lenses whereas electron beam is focused by electromagnetic lenses which consist of copper wire coils (Figure 23). By changing the magnetic field in the coils, the electron beam is manipulated [35].

There are many signals which can be detected based on the operating mode of the microscope, when the electron beam collides with a specimen. Two types of the electron signals are of our interest: Backscattered electrons (BSE) and Secondary electrons (SE). Backscattered electrons (BSE) are electrons from the primary beam, the electron beam collides elastically (no energy lose) with the specimen. BSE are used to create images showing the compositional contrast based on an elements atomic number [38]. The interaction with heavy elements is strong therefore it results in brighter areas than the interaction with light elements [35]. Secondary electrons (SE) used to investigate surface morphology. Figure 25.a shows a schematic diagram of these interactions [35]. Figure 25.b shows the difference between BSE images and SE images.

The volume of interaction between the beam and the specimen is called the interaction volume is pear-shaped [35]. This volume depends mainly on electron beam voltage and materials atomic number (Z). It is proportionally related to electron beam energy and inversely proportionally to Z [39]. Figure 26.a describes this interaction [38] and Figure 26.b describes beam penetration.

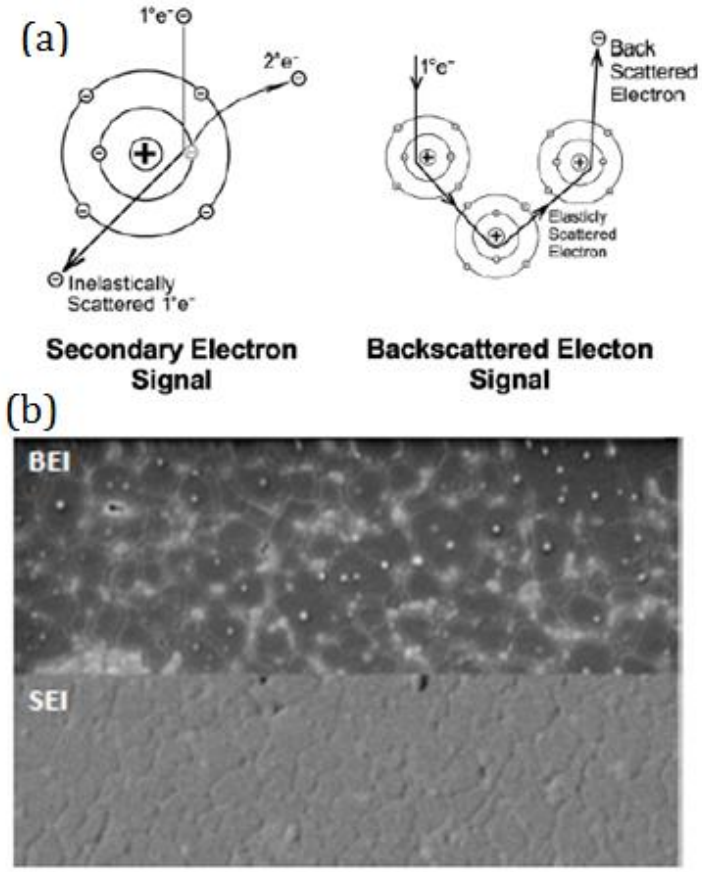

Figure 25: (a) Schematic of secondary electron and backscattered electron. (b) SEM images of the SE image (on the bottom) shows surface roughness of the sample while the BSE image (on the top) shows sample composition [35].

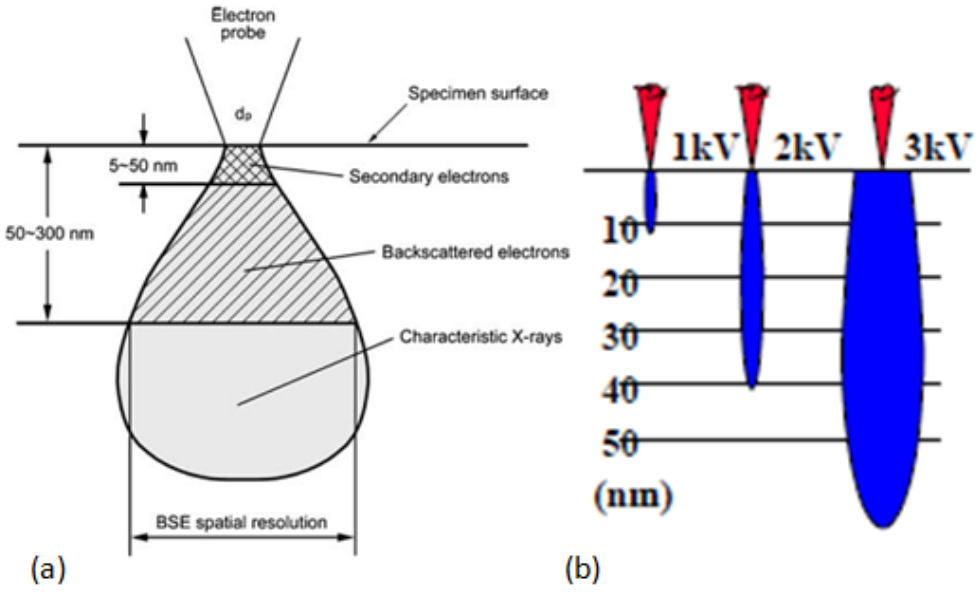

Figure 26: (a) Interaction volume. (b) Interaction depth dependant on electron beam energy [35].

BSE can go to deeper depth (50-300nm) and come up from the specimen because they have large energy. Whereas SE comes out through smaller depth (5-50nm) since their energy is low [38]. The BSE energy basically is beam energy which ranges from 1-30kV but SE energy ranges from 10-50eV [40].

Semiconductor detectors and Scintillator photo-multiplier detectors are used to detect BSE and SE, respectively [35].

The energy dispersive x-ray spectroscopic technique is used to indentify a specimen chemical compostion. Core electrons are excited to the conduction band by the electron beam therefore, a hole is created in the ground state. This hole is filled by an electron moved from a higher energy state [37]. As a resultant of this moving, x-ray waves are emitted because the electron moved from a higher energy

state to a lower one [37]. Figure 27 is schematic explains EDS [35]. Figure 28 is an example of EDS specter attached to the spot area image

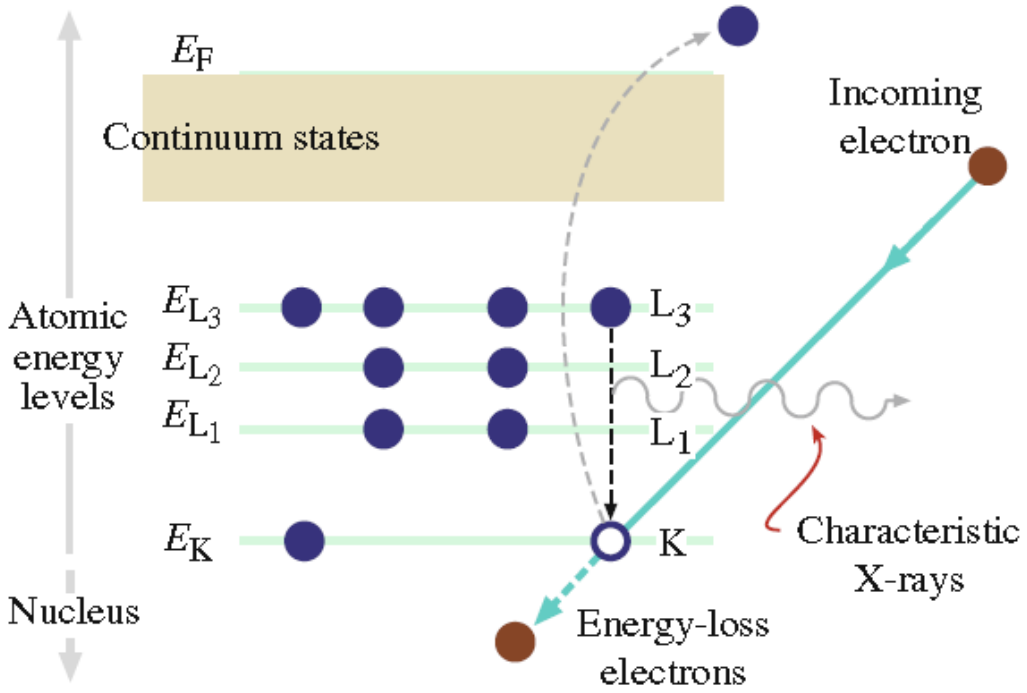

Figure 27: Schematic explains EDS [35].

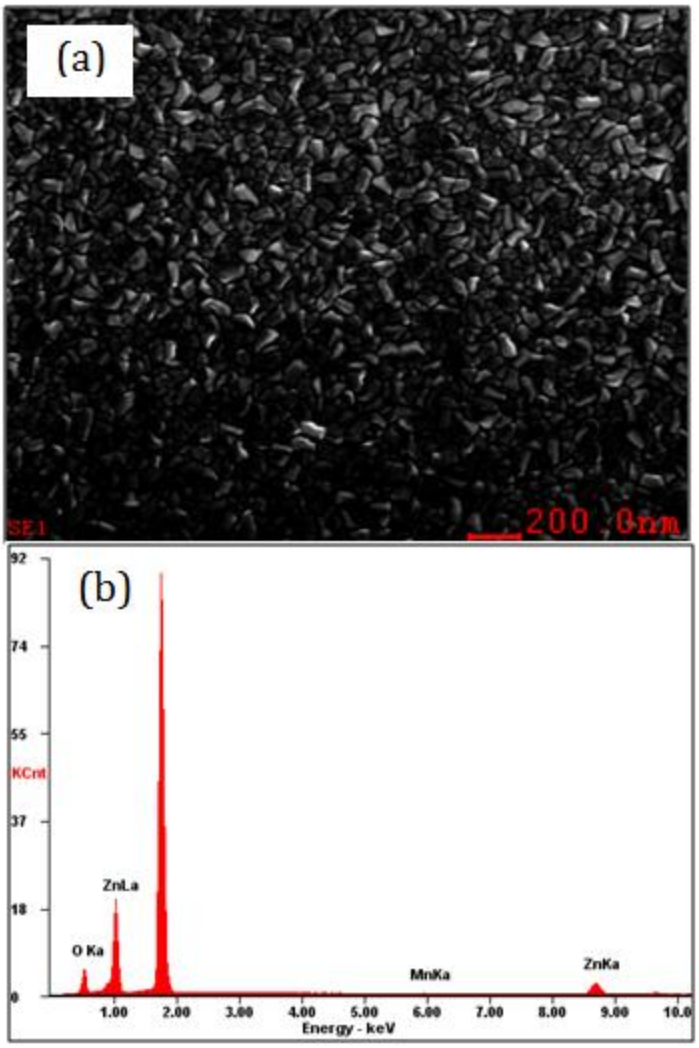

Figure 28: Example of EDS spectra attached to the spot area image [35].

3.3 Magnetization measurement procedure

This section will present how magnetization measurements are conducted and analyzed using the superconducting quantum interference device (SQUID) vibrating sample magnetometer (VSM) manufacture by QuantumDesign. This technique was invented by Foner in (the mid of 1960s). The basic idea of the SQUID

VSM is that the sample vibrates and creates a voltage; the voltage is amplified and measured.

3.3.1 SQUID VSM technique

The sample is inserted inside detection coils and is mechanically vibrated. The sample should be in the center surrounded by the superconducting coils as shown in Figure 29 [41]. These detection coils are superconducting coils which are designed to generate current only from the inserted sample magnetic moment [41]. The SQUID detector is a Josephson junction (JJ) which is a device based on electron quantum tunneling effect [42]. This effect states that there is a probability that a particle with lower energy can pass a barrier of higher energy [43]. This junction is made of superconducting wires and is connected to the detection coils, as shown in Figure 29. A voltage in the detection coils is created from this vibration and adds a current to JJ which is displayed in the screen in terms of magnetic moment. Equations (13), (14) and (15) represent this schematic [41].

$$V(z) = Az^2 \quad (13)$$

$$z(t) = Bsin(\omega t) \quad (14)$$

$$V(t) = AB^2 sin^2(\omega t) \quad (15)$$

Where V is the induced voltage by the sample, z is sample position, A is a scaling factor of sample magnetic moment, B is vibration amplitude, ω is vibration frequency and t is the time. Figure 29 is a schematic of SQIUD VSM system. Figure 30 shows SQUID VSM component.

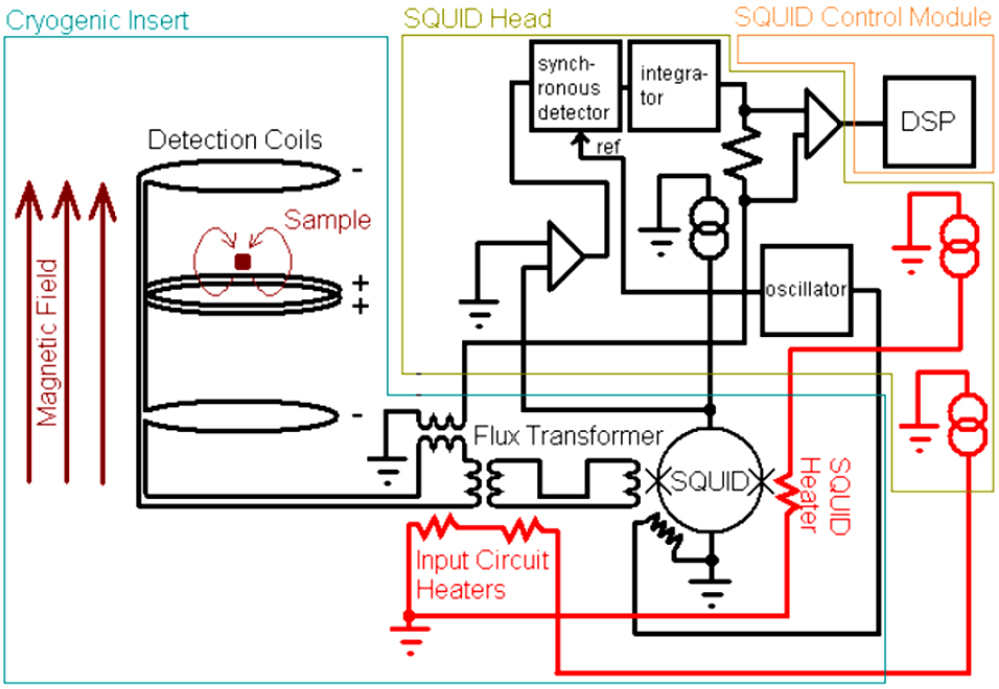

Figure 29: Schematic of SQIUD VSM system [41].

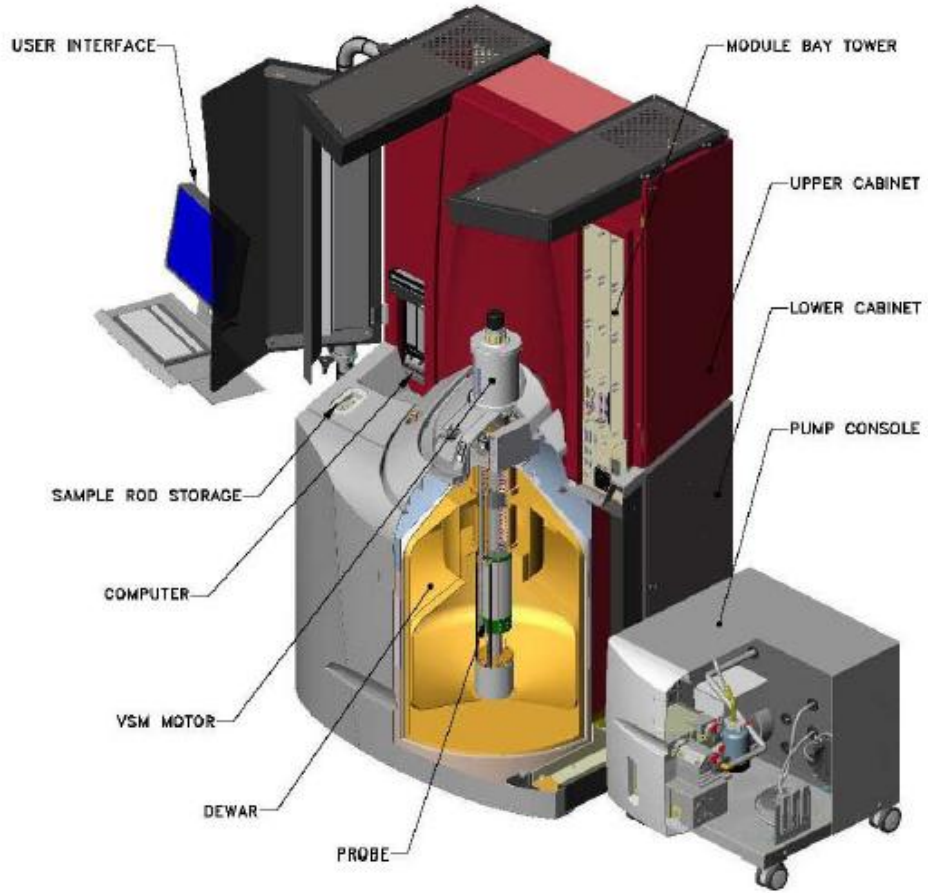

Figure 30: Shows SQUID VSM component [41].

3.3.2 Operation procedure

The SQUID measurement procedure can be explained in two steps:

A. Sample loading

The sample is fixed in the sample holder by G.E. (general electric) varnish glow because this glow has no significant magnetic signals, and sustains at low and high temperature. The sample holder is made from quartz. Brass and straw sample holders are also available. Sample holder types should be identified to SQUID

software by the user so its magnetization is automatically subtracted. Figure 31 shows the sample holder (yellow rod), sample base (red) and the insertion rod. Waiting time of 10-15 minutes is needed to dry the glow. The sample should be centered in the middle of the holder as indicated in the holder base in (Figure 31). Then the sample is fixed into an insertion rod which is 1m in height and inserted carefully in the SQUID dewar. Figure 32 shows a schematic showing the rod insertion process and KAUST SQUID VSM.

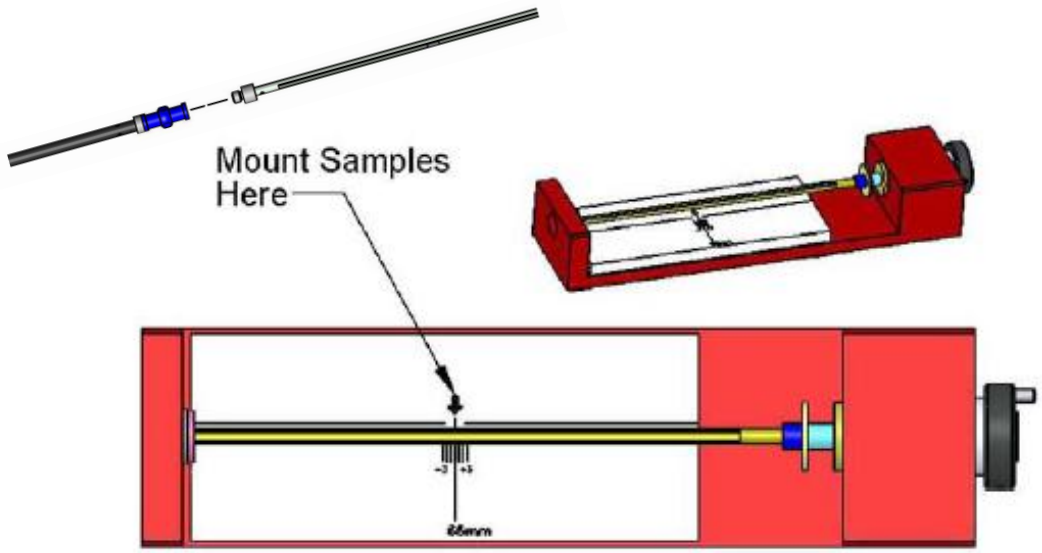

Figure 31: SQUID Sample holder and its base, and inserting rod in the top [41].

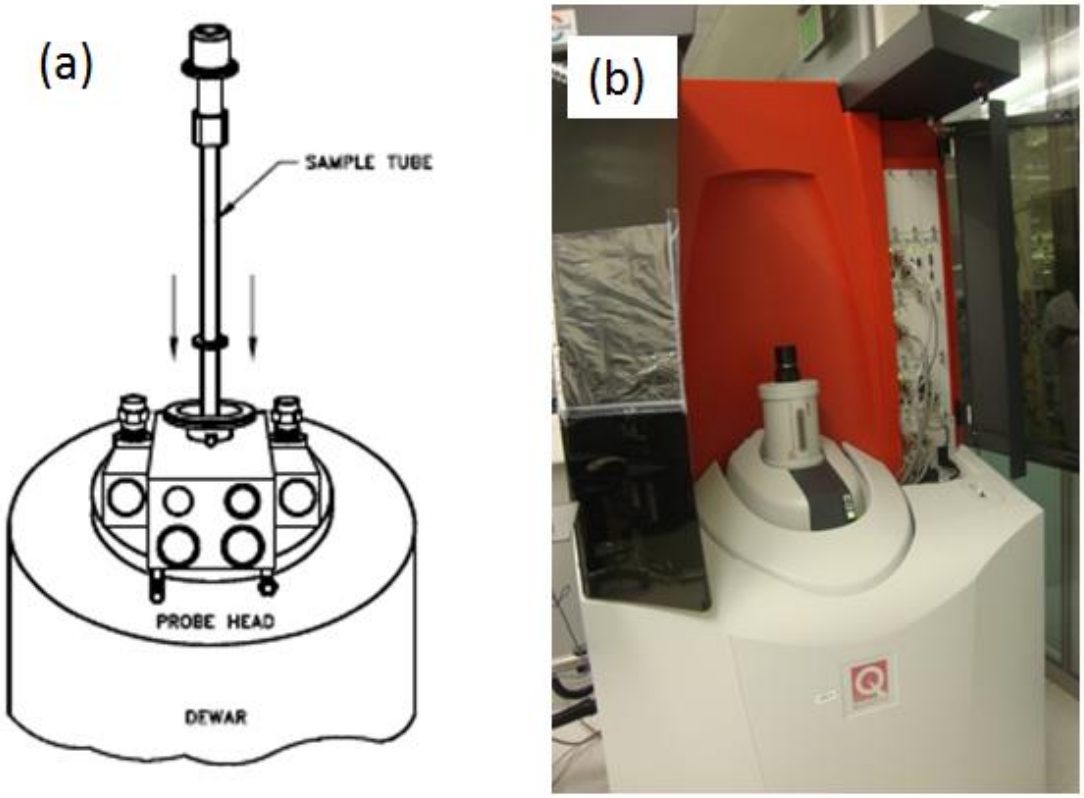

Figure 32: (a) Schematic of inserting the rod [41]. (b) KAUST SQUID VSM

B. Sample centering inside the SQUID

The sample position should be in the center of the detection coils to cancel the coils magnetic field as shown in Figure 33. Applied fields (e.g. 50, 100,500, -500Oe) are usually used to locate and center the sample. The center position is written in the holder base and the signal should match it.

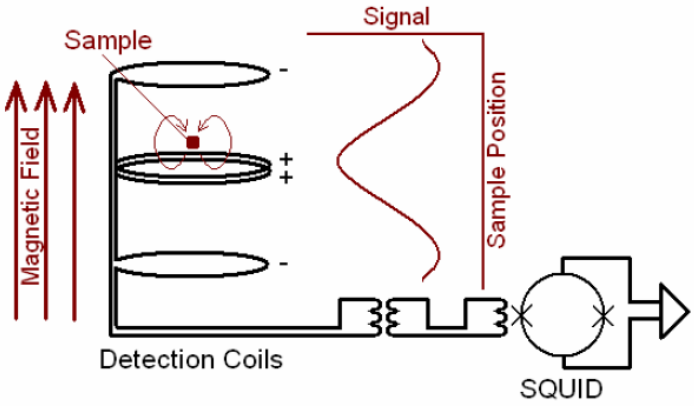

Figure 33: Sample centering [41].

3.3.3 Measurement sequence

There are three types of sequences commonly used for this measurement:

A. ZFC

Zero field cooled (ZFC) means that the sample is cooled normally to 5K and then heated to room temperature or higher while measuring its magnetization during heating. No magnetic field is applied, however, it is appropriate sometimes to apply small field (e.g. 20 or -20 Oe) to start the measurement with zero initial magnetization. It measures sample magnetic moment verses temperature to be used along with field cooling curve to identify and confirm sample magnetization type (e.g. ferromagnetic, paramagnetic, etc.).

B. FC

Field cooling (FC) measures the magnetization verses the temperature like ZFC but with an applied field. This applied field ranges from 100 Oe up to 1000 Oe. Another equivalent measurement is field cooled warming FCW. In FC, sample is

cooled whereas in FCW sample is heated. Figure 34 shows the ZFC and FC curves [44].

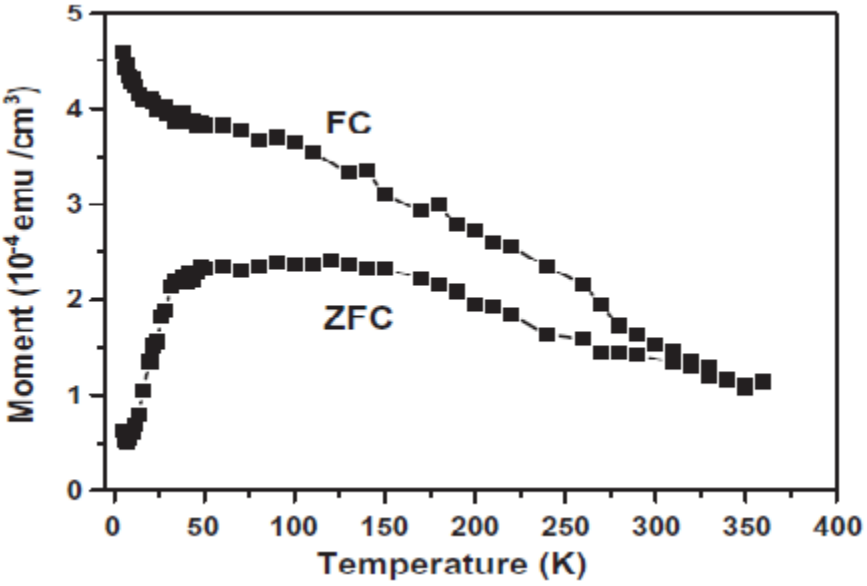

Figure 34: FC and ZFC curves for ferromagnetic material [44].

C. MH loop

The Magnetization verses the applied magnetic field (M-H) loop (or hysteresis loop) is the most important measured curve because it contains many magnetic values. Based on the shape of the hysteresis loop the magnetization type is identified. Figure 35 shows an MH loop of a ferromagnetic material.

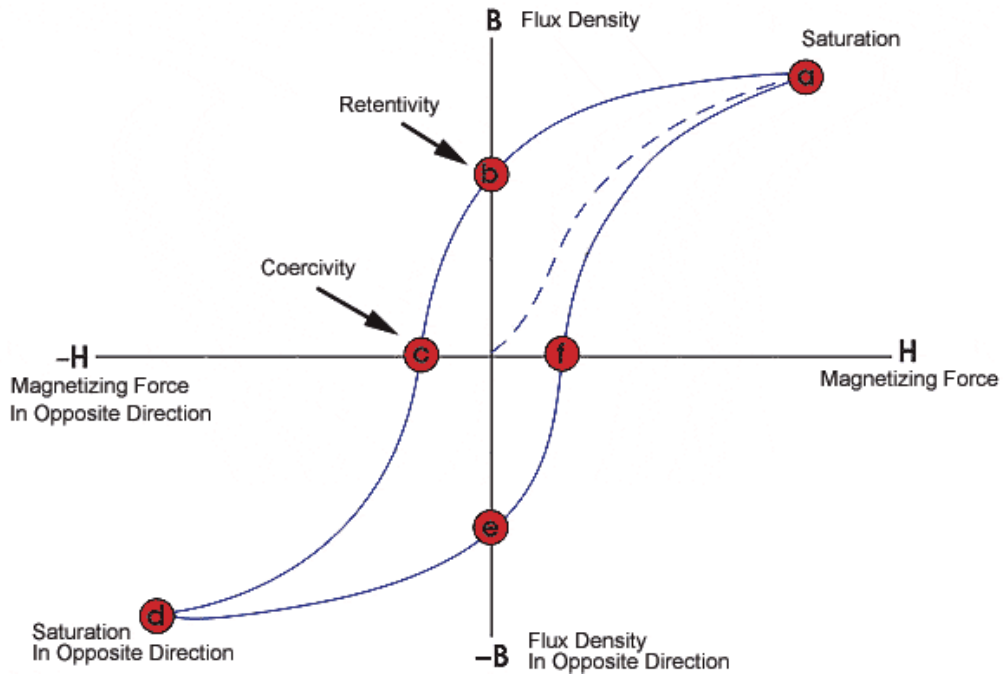

Figure 35: MH loop of a ferromagnetic material [45].

3.3.4 SQUID Data Analysis

The magnetic measurement of MH loop at certain temperature starts with applying magnetic field from 0 to 5 or 7 Tesla. The increment of the applied field depends on how many measurements have been written in the sequences. Figure 35 shows a typical hysteresis loop of a ferromagnetic material [45]. The dash line shows that the material has no spontaneous magnetization because the first measurement is zero. As the applied field increases, the curve reaches point *a* which is called the maximum saturation magnetization (M_s) [45]. M_s means that most of the magnetic domains of the material have been aligned with the direction of the applied field [45]. A magnetic domain is a small region inside the materials consisting of a trillion atoms or more with their moments aligned spontaneously in

one direction [45]. Point *b* and *c* in the curve are the important points during demagnetization. Point *b* represents the remanence, also called retentivity, of the materials which is the sustained magnetization in the material after removing the applied field [45]. Point *c* represents the coercivity which is a measure of the required applied flied to make the net magnetization of the domains equals to zero [45].

3.4 Deposition technique

Pulsed laser deposition (PLD) was used to deposit the films. It was used because it is the most common technique used to grow Mn doped ZnO thin films, high quality ferromagnetic and semiconductor films can be grown and it is available at KAUST. Moreover, the deposition conditions of the PLD can be easily controlled. In the PLD a high energy beam impacts onto a target and ablates target particles creating a bloom of these particles. Then, these particles are deposited in the substrate [46]. Figure 36 shows a schematic of the PLD.

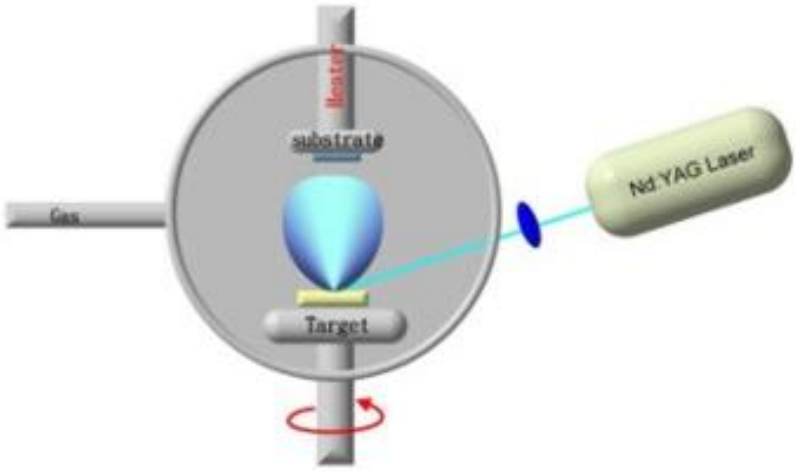

Figure 36: Schematic of the PLD [46].

Chapter 4 Results

In this chapter the experimental work and characterization results are presented. The experimental work includes target preparation and deposition conditions. The structural properties are investigated using XRD and SEM, and the magnetic properties are carried out by using the SQUID VSM.

4.1 Target preparation

Films composition and quality is highly dependent on target preparation [12, 19]. Sintering the target above certain temperature suppressed ferromagnetism as shown in (Figure 37) [12]. Target preparation includes: materials quantity, powder mixing, calcinations, pressing and sintering. Optimized conditions of the previous steps differ from material to material or compound as we observe from the literature. As the target consists of several materials and compounds, optimizing these condition are hard to get. Moreover, a detailed procedure of the preparation is usually not mentioned in many papers, where “standard solid state route” is the common phrase used in the literature. However, common rules are known and no precise values are needed to prepare the targets. One of them is that the sintering temperature which should not exceed the melting point of target materials. In addition, Film compositions are not usually the same as the target composition [12]. The deposition conditions play a crucial role on thin films. $Mn_{0.02}Zn_{0.98}O$ target was prepared because it is used extensively in the literature where some researchers report its room temperature ferromagnetism as well as some reported that it is not FM.

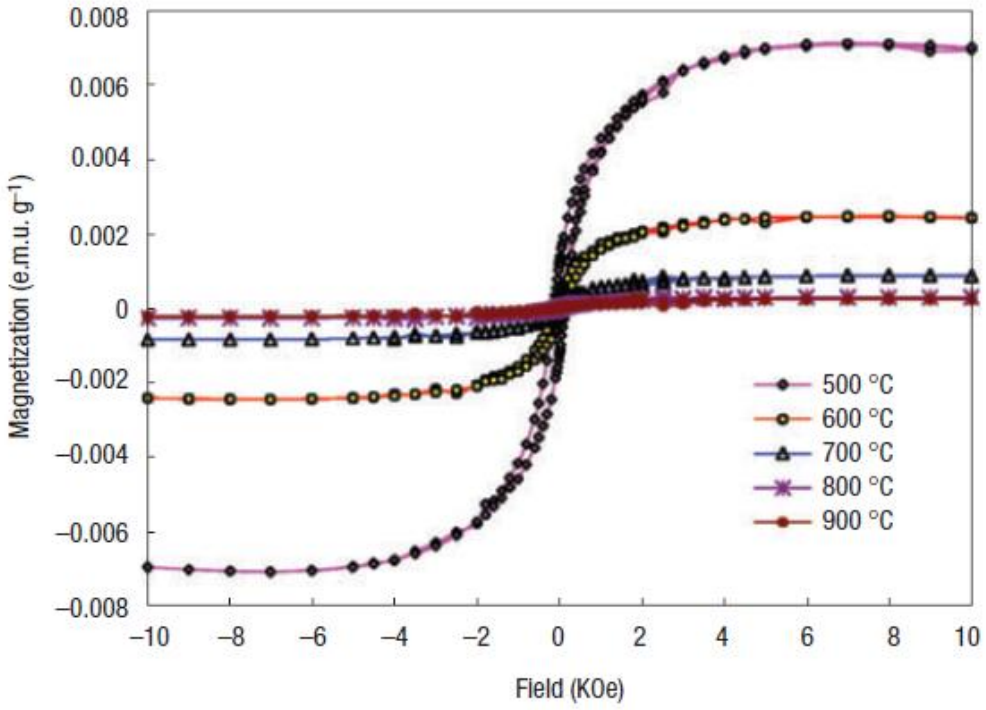

Figure 37: M-H loops at room temperature for 2 at.% Mn doped ZnO pallets. These pallets have been sintered at various temperatures. Pallets sintered above 700˚C did not show ferromagnetism [12].

The target preparation was as follows: The required amount of the materials were calculated based on the atomic weights ignoring oxygen weights because it is difficult to control it since the mixing is in normal air and the deposition is in oxygen environment. The precursors were ZnO and Mn_2O_3 powders and were 99.99% pure from Sigma-Aldrich. Mn in the compound it is Mn_2 so the molecular weight (MW) should be multiplied by 0.01 instead of 0.02 because of the two. In addition to the required compound weight percentage, target size is an important matter to choose. For 1 inch diameter target less than 10g are enough. The powders were mixed and

ground (Figure 38) by agate mortar for 3 hours. During grinding, particles become finer with the time. The ZnO powder is shiny white while Mn_2O_3 is black. Although MnO powder was in a very small amount, 2%, in the end of grinding the mixture is no more shiny. After that, the mixture was calcined at 300˚C for 10 hours. Calcination (heating) temperature and time affect phase transformation and particle size [47]. Then, the mixture was ground again for 3 hours. The powder was pressed at 4 ton for 10 min. Finally, the target was sintered at 500˚C for 10 hours. The target was white color as shown in Figure 38.

Figure 38: Agate mortar and pestle (gray), and the crucible used for sintering

4.2 Growth conditions

There are many conditions that can be manipulated in the PLD. These conditions are: substrate temperature, oxygen pressure, number of pulses, beam energy, frequency of pulses, the distance between the target and the substrate, and

beam laser type. Also beside that, substrate type is very important. Table 3 shows a literature review of Mn doped ZnO PLD conditions [9, 12, 19, 33, 48-53].

Table 3: Growth condition of Mn doped ZnO from various references

Mn at. %	Substrate	Temperature (C)	P_0 (mTorr)	Frequency (Hz)	Results of M_S	Ref.
5	c-sapphire	500	_	10	0.08 emu/cm3	[51]
5	c-sapphire	700	_	10	2.55 emu/cm3	[51]
30	c-sapphire	700	1 x 10^4			[52]
30	c-sapphire	800	1 x 10^6			[52]
2	c-sapphire	400	200	10		[12]
0.1-35	c-sapphire	600	5X10^-5	10		[48]
10	c-sapphire		10^-6		0.9 emu/g	[9]
30	c-sapphire				3.4 emu/g	[9]
<35	c-sapphire			5		[53]
3, 10, and 22	c-sapphire	550	0.02		0.013 emu/g for 6.5 %	[19]
5-25	a- Al_2O_3 (1120)	350-600	2-4 x 10^-2			[33]
0.02	c-sapphire	800	400			[50]
0.1-1	c-sapphire	400 -600	20	1		[49]

The PLD model at KAUST is NEOCERA and the laser is Coherent complex pro-Krf (λ= 248 nm). Based on Table 3, we used optimized conditions for our films

which are: substrate temperature of 600◦C, beam energy of 250 mJ with laser frequency of 10 Hz and at different oxygen pressures (50mTorr, 300 mTorr and 500 mTorr). Moreover, the films were deposited on different substrates: Al_2O_3 (0001), Al_2O_3 (1102) and silicon.

4.3 XRD Results

The XRD results show the change in lattice parameters and peak positions due to changing oxygen pressure (P_O), the film quality and the XRD spectra peak designations. The XRD measurements were carried using the core lab facilities (Bruker DISCOVER 8 Thin film).

4.3.1 Lattice parameters

XRD data reveals the change that occurs to doped ZnO films compared to pure ZnO films. Table 4 shows our calculated lattice parameters for our PLD pure (undoped) ZnO and Mn doped ZnO thin films. Whereas

Table 5 shows the full width half maximum (FWHM) of (002) peak of ZnO for ZnO films deposited on c-sapphire. The width of XRD peak (i.e. FWHM) is an indication of materials quality, smaller FWHM value indicates higher quality. Most of the FWHM values are less than 0.2° which indicate high quality c-axis orientation [34]. Quality here means more crystals prefer to grow at a specific direction. Film

quality increased as oxygen deposition pressure (Po) increased for pure ZnO as shown in

Table 5. Mn doped ZnO film deposited at 300mTorr showed the worst quality because its FWHM was very large. We seek optimum conditions to be used in growing films of different concentrations. Among different substrates, R-cut sapphire showed the best quality, as shown in

Table 6. Different substrate orientations resulted in different lattice parameters [54].

Table 4: Lattice parameters for pureZnO and Mn doped ZnO as determined from XRD measurements

	P_O	**2 θ**	**c (nm)**	**a (nm)**
Mn Doped	50mtorr	34.56	0.519	0.300
Mn Doped	300	34.33	0.522	0.302
Mn Doped	500	34.63	0.518	0.299
Pure	50mtorr	34.6	0.518	0.299
Pure	300	34.63	0.518	0.299
Pure	500	34.64	0.518	0.299
Theoretical		34.42	0.521	0.301

Table 5: Change in FWHM of (002) peak of ZnO for the films deposited on c-sapphire.

Oxygen pressure	50mTorr	300mTorr	500mTorr
Pure ZnO	0.2165°	0.1983°	0.1721°
Mn Doped ZnO	0.1806°	0.4570°	0.1764°

Table 6: Change in FWHM of (002) peak of ZnO for the films deposited on different substrates at 500mTorr

	c-sapphire	R- cut sapphire	Silicon
Doped ZnO	0.1764°	0.1516°	0.2834°

4.3.2 Peaks shifts

Table 7 shows a comparison of (002) 2 θ peak positions between the pure and doped ZnO films with changing the P_O as shown in Figure 39 and Table 7 as well.

Table 7: Change in (002) ZnO peak position for Mn doped ZnO compared with pure ZnO films

	50mTorr	300mTorr	500mTorr
Pure ZnO	34.6°	34.63°	34.64°
Doped ZnO	34.56°	34.33°	34.63°

Figure 38 shows pure ZnO, (002) peaks that shift to the right as Po increases (see Table 7). This means smaller c parameter ($c = \frac{\lambda}{\sqrt{3}Sin\theta}$), therefore a decrease in the crystal sizes.

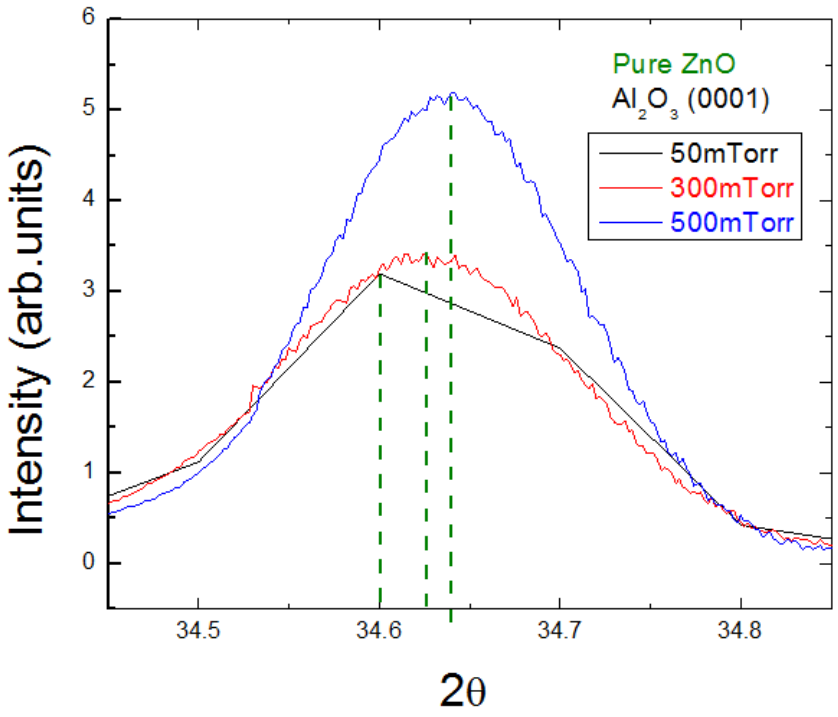

Figure 39: Peak shifts with varying Po for pure ZnO films.

For Mn doped Films, the film deposited at 500mTorr has a 2θ value close to that of the pure ZnO film as shown in Table 7, which indicates that a very slight change occurs in the lattice parameters due to doping (only 0.002nm for *c-axis*). Since the (002) peak position is associated to the c lattice parameter, 300mTorr doped film had the smallest 2θ (34.33°) therefore it has the largest crystals.

Mn doped ZnO films, the 2θ value of (002) peak smaller than the pure ZnO films, Table 7 and Figure 40. This indicates an expansion in the lattice. this

expansion may be due to Mn replacement and covalent bond [55]. Zn radius is larger than Mn radius; therefore, if Mn replaced Zn lattice should shrink. Although this is opposite of our assumption that the lattice expands with Mn dopants, the covalent radius is accounted and Mn covalent radius is larger than Zn [55]. Table 8 supports our assumption.

Table 8: Zn and Mn atomic and covalent radii values [56].

	Atomic radius (pm)	Covalent radius (pm)
Zn	142	131
Mn	127	139
Effect of Mn replacement of Zn	Lattice will shrink	Lattice will expand

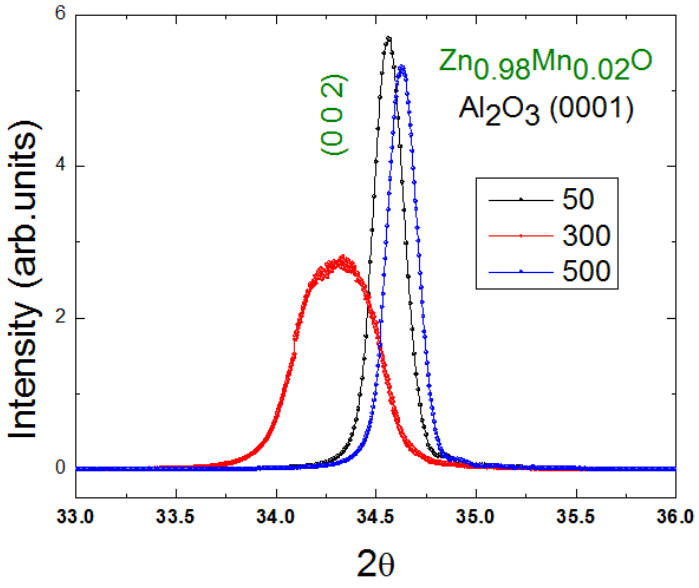

Figure 40: Mn doped ZnO peak positions

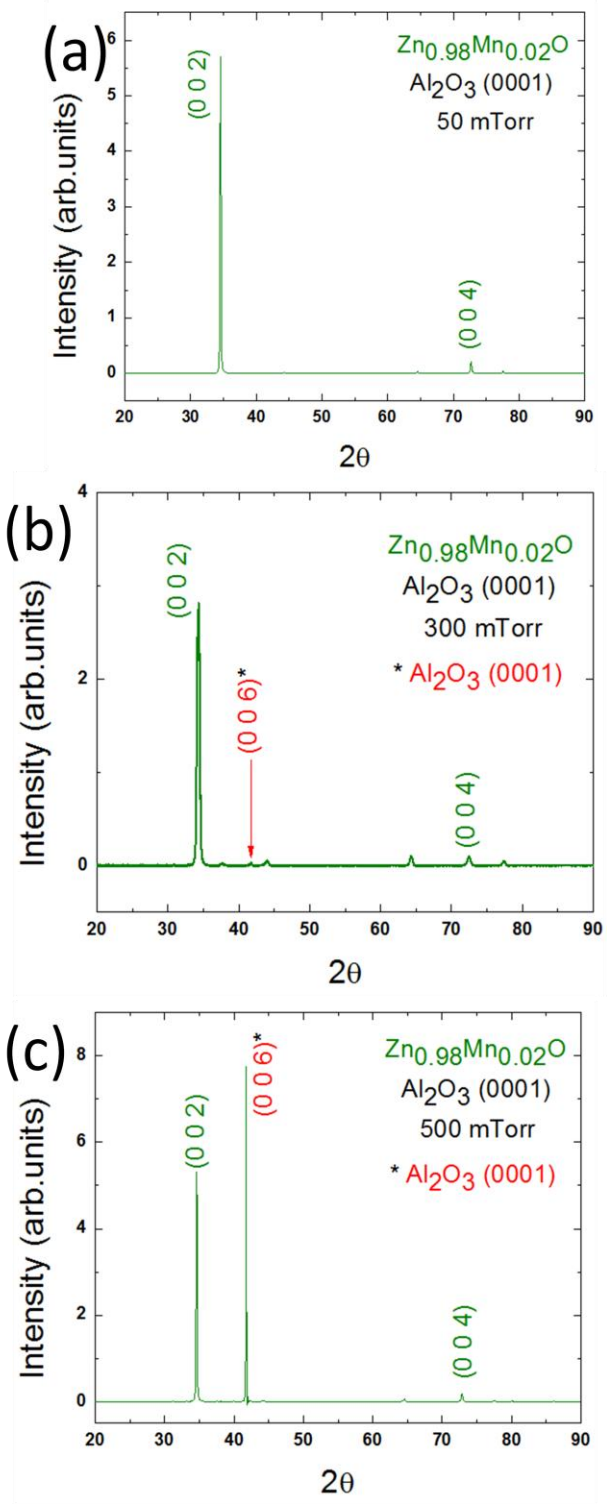

Figure 41: XRD spectra for pure ZnO deposited at (a) 50 mTorr, (b) 300 mTorr and (c) 500 mTorr.

4.3.3 Peak designation

Peaks were designated by comparing our data with the international center of diffraction data (ICDD) that is obtained from the core lab PC. The XRD spectra were θ-2 θ scan at selected ϕ angle in order to minimize Al_2O_3 substrate peak. Firstly, a comparison between pure ZnO films and hexagonal ZnO was conducted. For all ZnO and ZnMnO films, (002) peak was the dominant XRD peak in addition to a small peak of (004) as shown in Figure 39. This indicates that the grown films are hexagonal. However, two peaks at 44.3° and 64.5° were shown in the pure and doped samples. Lee et al. [57], reported a peak at approximately 44.3° for zinc blende ZnO on c-sapphire [57]; further investigation should be done to study the origin of these peaks . No secondary phases were detected in Mn doped ZnO, though it should be noted that XRD has a limitation to detect phases which are less than 2% abundance.

4.4 SEM Results

The SEM results include surface analysis, thickness measurement and chemical composition analysis. The measurements were carried out using KAUST SEM located in the core lab (FEI Helios 400S)

4.4.1 Surfaces comparison

SEM images of Mn doped ZnO films in Figure 42 show that grain size increases as deposition oxygen pressure (P_O) increases. Higher oxygen pressure causes more collision between oxygen atoms and ablated particles from the target.

Hence, formed grains became larger [58]. Dark areas in 50mTorr film indicate the grains with lower height.

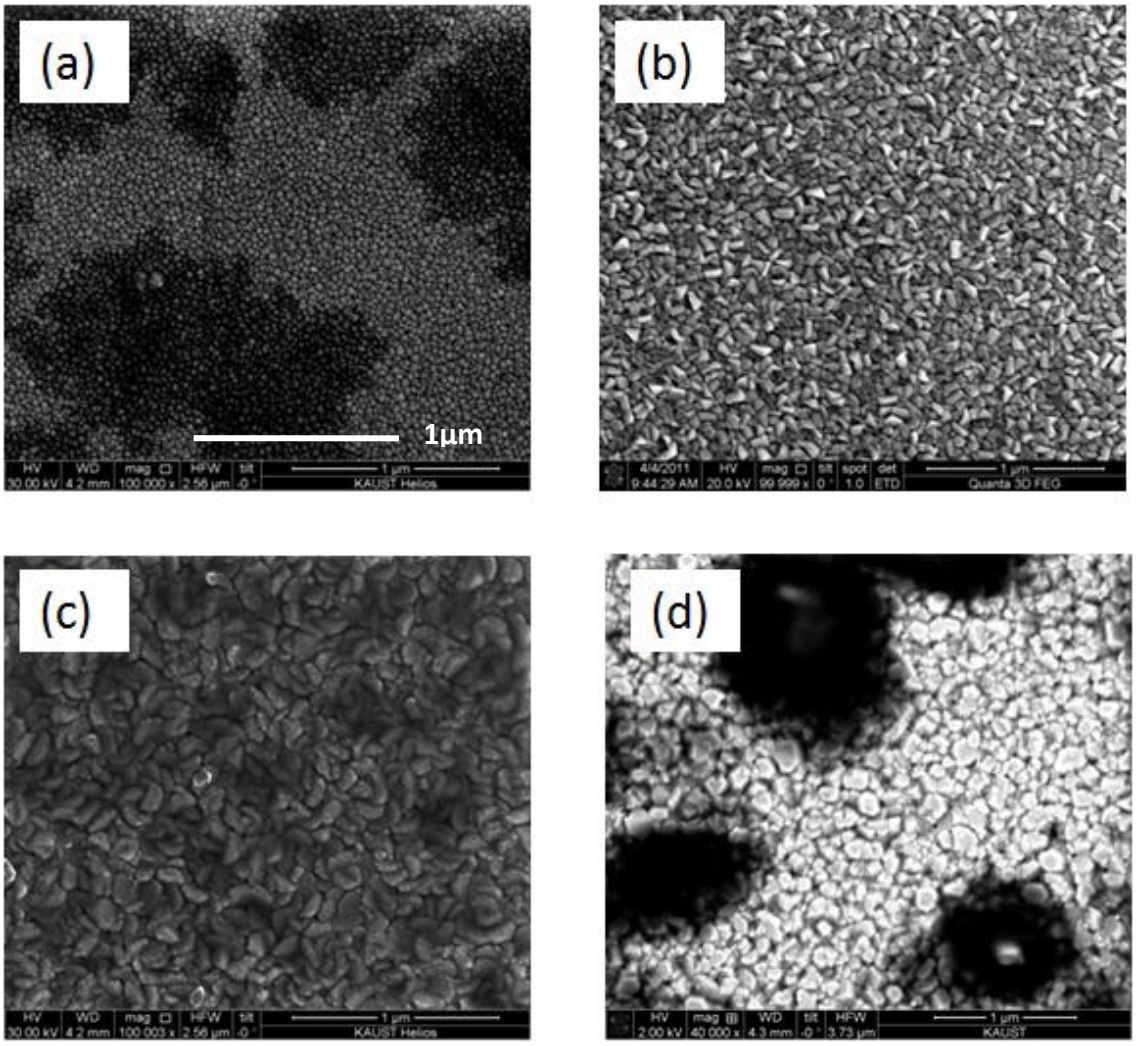

Figure 42: The SEM images for Mn doped ZnO films deposited at different P_O, a) at 50 mTorr, (b) at 300 mTorr, (c) at 500 mTorr and (d) Pure ZnO deposited at 500mTorr.

Film thickness was measured by SEM using the secondary electrons signal. Films were tilted 52˚ to measure the thickness of the films. The calculated number shown in the image is the true one. Table 9 shows film thickness increases as P_O

increases in Mn doped ZnO films. Figure 43, shows the thickness difference between 300mTorr film (Figure 43.a) and 500mTorr (Figure 43.b). The film deposited at 500mTorr on Si substrate shows different thicknesses (222 to 260 nm) as shown in Figure 43.b.

Table 9: Variation of film thickness of Mn doped ZnO film with oxygen pressure change

oxygen pressure	50mTorr	300mTorr	500mTorr
Film thickness (nm) for Mn doped ZnO	185	203	247

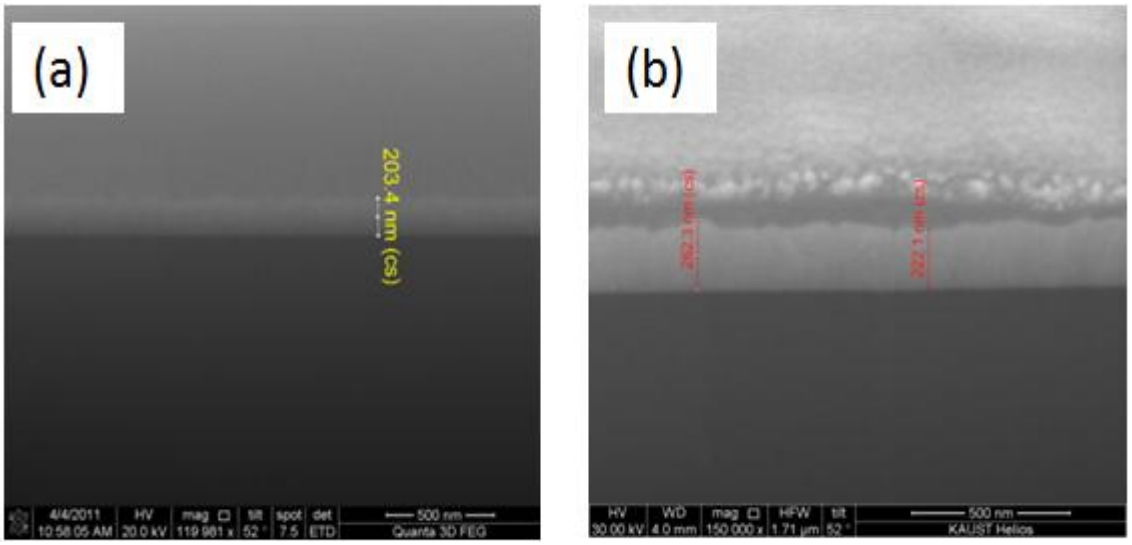

Figure 43: SEM images show Mn doped ZnO thickness for different P_O. a) 300mTorr and b) 500 mTorr.

For pure ZnO and Mn doped ZnO films deposited at P_O = 500mTorr, we observed that the average thickness of the Mn doped ZnO film (247nm) is much

higher than the pure one (183nm). The Mn covalent radius which is accounted during deposition is greater than Zn covalent radius [55]. We proposed that Mn may be replaced Zn site and this expands the lattice size. Therefore, the thickness was increased with Mn dopants.

4.4.2 Elemental Mapping and Energy dispersive x-ray spectroscopy (EDS)

Figure 44 indicates that the elemental mapping obtained by using EDS attached to SEM showed that the distribution of Zn, O, and Mn are uniform for all Mn doped ZnO films deposited on Si.

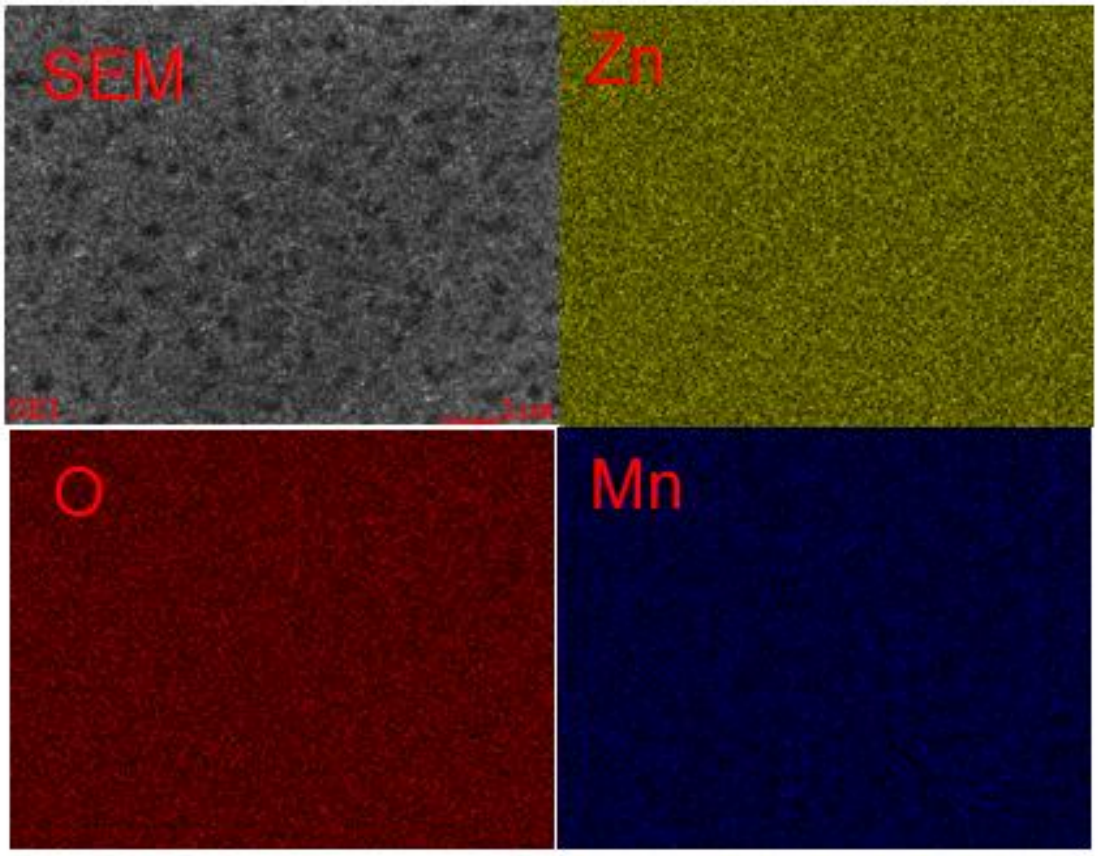

Figure 44: EDS shows that the distribution of Zn, O, and Mn are uniform.

Table 10 shows that Mn concentration decreased as P_O increases. The atomic weight was less than 1% whereas the target contains 2% Mn. However, we have repeated the measurement to confirm the results but we obtained different values. Further measurement for determining the concentration of Mn in the film (e.g., Wavelength Dispersive X-ray analysis (WDX)) is needed. Moreover, EDS is a qualitative tool and not quantitative so it is not accurate.

Table 10: Mn atomic weight measured using EDS for Mn doped ZnO on Si substrate at different pressures.

oxygen pressure	50mTorr	300mTorr	500mTorr
Mn atomic weight %	00.66	00.55	00.41

4.5 Summary of the structural properties

While pure ZnO films deposited at different P_O showed no change in lattice constants, the Mn doped ZnO showed a change in the lattice parameters. As P_O decreases Mn concentration increases and lattice parameters increases. This proposes that Mn replaced Zn.

4.6 Magnetization measurement results

Magnetization measurements on our thin films were carried out by using MPMS SQUID VSM (Quantum Design). The diamagnetic substrate effect was subtracted and data were plotted using the 'OriginPro 8.5' software. The MH loops at 5K and 300K, and the zero field cooled (ZFC) and field cooled (FC) magnetization data are shown in this section. The saturation magnetization (M_S), remanant magnetization (M_R) and coercive field (H_C) values are reported. Although our films were deposited on c-cut and R-cut sapphire substrates, interestingly, their magnetic results were roughly similar. Therefore, only the results on those films deposited on c-sapphire substrates are shown here. The inset in the MH figures shows a magnified central portion of the MH loops near the origin.

4.6.1 The 50mTorr ZnMnO films

The initial magnetization values (first quadrant in the MH loop) indicate that the sample has spontaneous magnetization. Room temperature ferromagnetism is observed in the film deposited at P_O =50 mTorr as shown in (Figure 45.a). At 300K, the M_S is 2.8 x 10^{-4} emu/g, M_R =4.4 x 10^{-5} emu/g and H_C= -69 Oe. The MH loop at 5K (Figure 45.b) shows an unsaturated magnetization behavior as the applied magnetic field increases up to 50 kOe. We propose that this behavior could be originated due to a co-existence of a ferromagnetic and a superparamagnetic secondary phase. Also, it is believed that a superparamagnetic phase is due to some percolation of clusters of single domain particles (FM and AFM). The magnetic ordering in such a single domain particle grows as temperature is lowered and is evidence from the

ZFC and FC magnetization data, (Figure 45.c). As the size of this cluster is assumed to be very small of the order of nanometers, it was not detected by XRD, XPS and SEM. To clarify this, high resolution TEM analyses are needed to be carried out at low temperature.

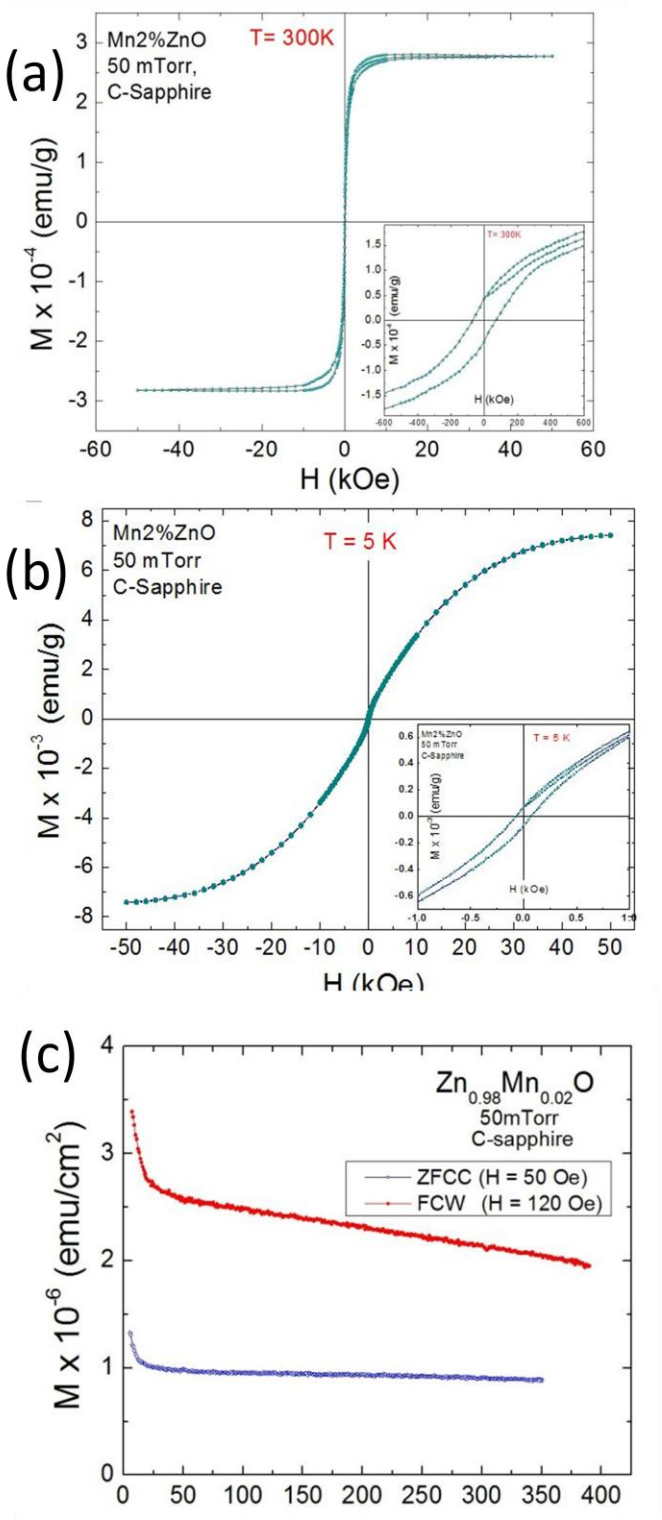

Figure 45: Mn doped ZnO at Po = 50 mTorr magnetization curves: (a) MH loop at 300 K, (b) MH loop at 5 k (c) MT curves (FC and ZFC)

4.6.2 300mTorr ZnMnO films

These films share similar properties of those deposited at 50 mTorr except that there is no initial magnetization in the MH loops (Figure 46.a). In addition, the M vs. T curve for this film shows a distinct Curie transition with a Curie temperature at 74 K, as shown in (Figure 46.c). This raises a lot of doubt since the MH loop at 300 k is showing FM. The question is how the MT curves show T_C at 74 k and the MH loop at 300 shows ferromagnetism? MH loops at different close temperature intervals around 74 K should be conducted to investigate this interesting results. At 300K, the M_S is 1.8 x 10^{-4} emu/g in the MH loop, M_R =3.2 x 10^{-5} emu/g and H_C= -105 Oe. More characterizations should be carried out to investigate this vague behavior. Worth mentioning here, that this films showed the worse film quality as seen from XRD pattern.

4.6.3 500 mTorr ZnMnO film:

These films also show a similar behavior of that observed in 50 mTorr films, (Figure 47). For MH loop at 300 K, M_S was 5.6 x 10^{-4} emu/g for MH loop at 300K, M_R =4.7 x 10^{-5} emu/g and H_C = -50 Oe.

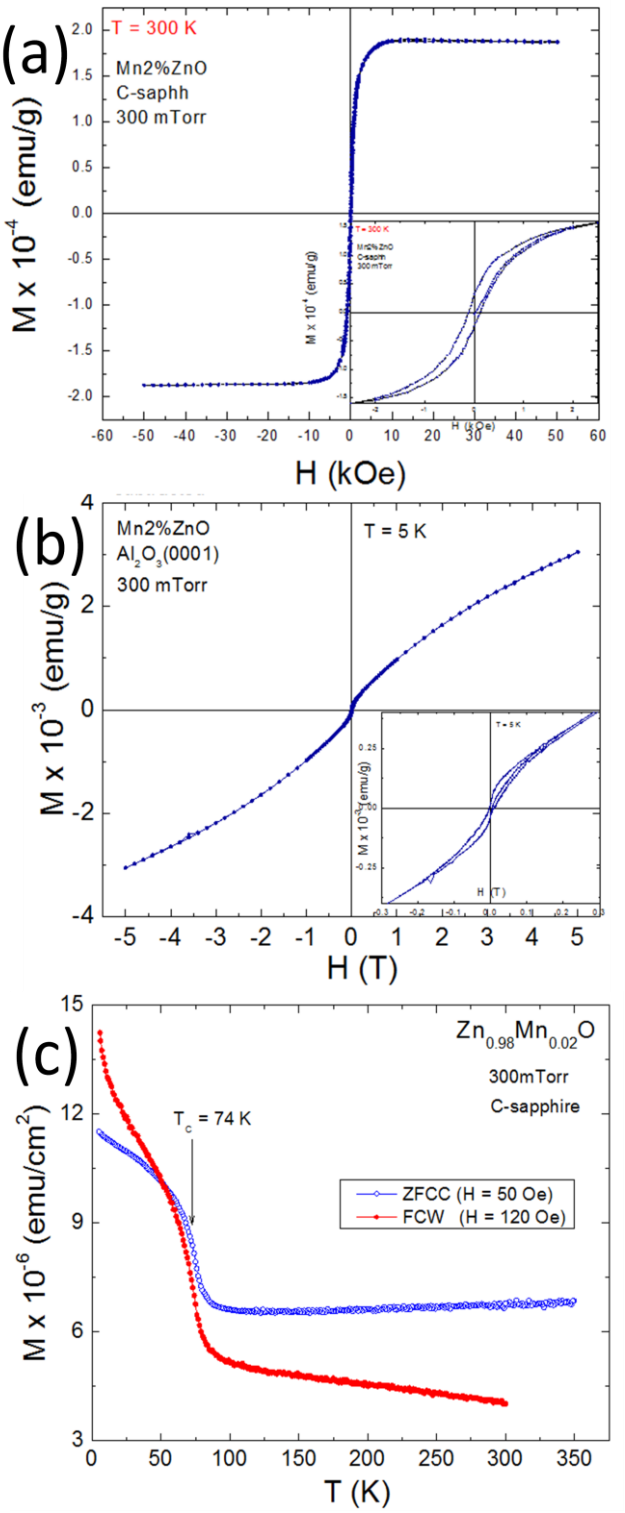

Figure 46: Mn doped ZnO at Po = 300 mTorr magnetization curves: (a) MH loop at 300 K, (b) MH loop at 5 k (c) MT curves (FC and ZFC).

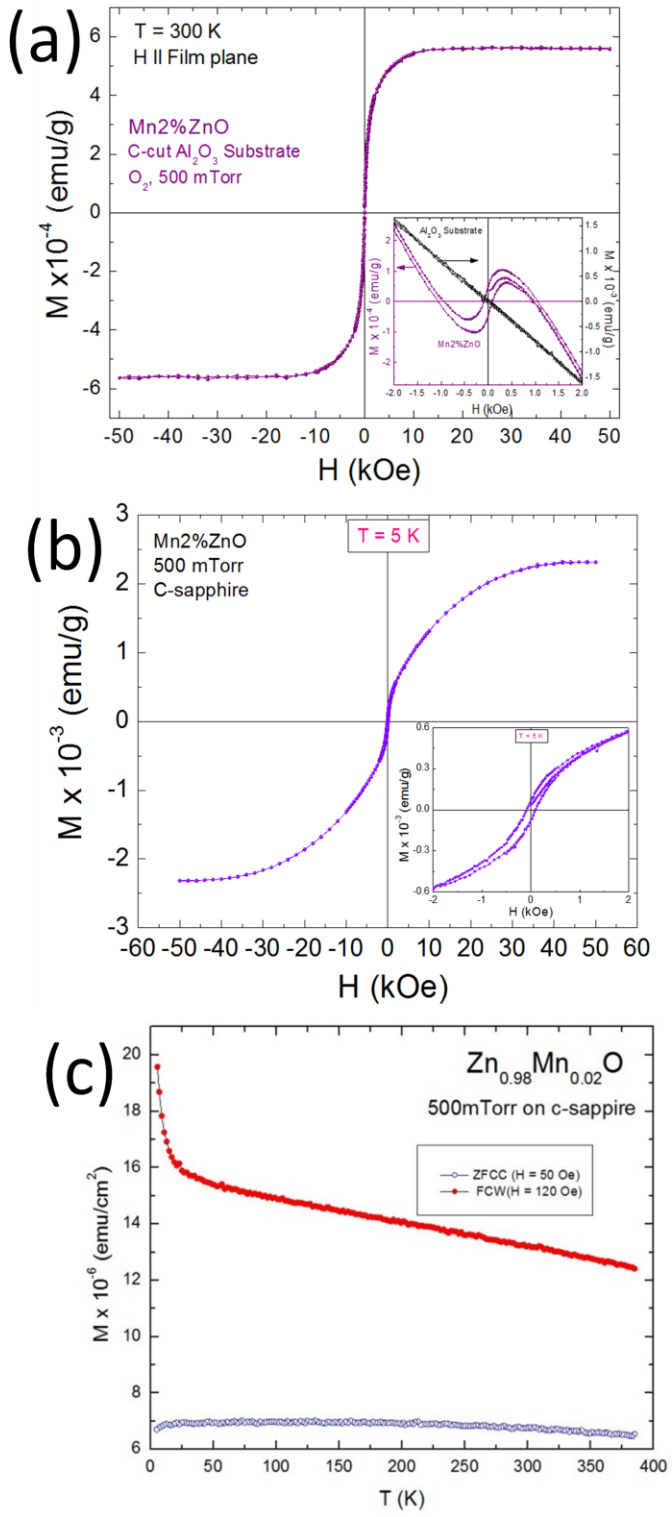

Figure 47: Mn doped ZnO at Po = 500 mTorr magnetization curves: (a) MH loop at 300 K, (b) MH loop at 5 k (c) MT curves (FC and ZFC)

4.6.4 Discussion of magnetization results

All the films deposited on c-sapphire substrates showed a ferromagnetic behavior at 300 K, whereas at 5K we observed a superposition of a ferromagnetic and another behavior which is possibly superparamagnetic. It is unusual to see FM at RT and another behavior at low temperature (such as paramagnetic). There are two possibilities of this unexpected behavior: First, the cause of this superparamagnetic behavior may be the existence of secondary phases. The possible secondary phases are Mn-oxides, Zn doped MnO, interacted Mn ions (clusters) or free Mn atoms. Mn oxides are anti-FM at low temperatures [31], interacted Mn ions could be FM or anti-FM based on the type of Mn states that interact with each other [59]. Free Mn ions are paramagnetic [60]. The second possible explanation of the superparamagnetic behavior at 5K that is Mn in ZnO may not contribute to the ferromagnetic behavior. Schoofs et al. [34] showed evidence that Mn in ZnO does not contribute to ferromagnetic moment by investigating the local coordination of the atom site inside the lattice using x-ray magnetic circular dichroism (XMCD) and X-ray Absorption. The ferromagnetism in Mn substituted ZnO may be originated from a defect complex such as Oxygen vacancies [21].

A similar behavior has been observed from Co doped ZnO to that which has been observed in our experiment [54]. Their theoretical calculations confirmed the XMCD results and showed that ZnCoO has a superparamagnetic behavior and Oxygen vacancies-Co pair. These results also showed a long range ferromagnetic order [61].

MT curves showed paramagnetic behavior for 50 mTorr and 500 mTorr films; while 300mTorr film showed ferromagnetic with TC less than 100 K, however MH curves showed FM at 300 K. These are unexpected results based on previous literatures of Mn doped ZnO). More M-H hysteris data at different temperatures (e.g. 50 K, 100 K and 200 K) should be done to track the change in magnetization verses temperature. these behaviors may have originated from defect complexes [27]. We exclude the Anti-FM from the Mn-oxides because $1/\chi$ curves showed that the films have no critical temperature, as known for paramagnetic materials [23].

A summary of the previous curves is shown in Table 11.

Table 11: Summary of magnetization results

	Type at 300 K	M_S at 300 K (emu/g)	M_R at 300 K (emu/g)	H_C at 300 K (Oe)
50mTorr	FM	2.8×10^{-4}	4.4×10^{-5}	69
300mTorr	FM	5.8×10^{-4}	-	-
500mTorr	FM	5.6×10^{-4}	4.7×10^{-5}	50

Chapter 5 Discussion and conclusion

In this chapter, a discussion of the previous results is presented with the aim of establishing a durable link between structural and magnetic properties in order to investigate the origin of ferromagnetism in Mn doped ZnO

The XRD results showed no change in c lattice parameter in pure ZnO films deposited at various P_O indicating no change in the lattice as a function of P_O. However, the FWHM values indicated a change in the quality of the pure ZnO films. For the Mn doped films there was a change in c parameter with changing P_O. The c parameters of the doped films are larger than those of pure ZnO which suggest that Mn has replaced Zn in the lattice [18].

The change in c parameters with Mn concentration is not proportional, i.e. it is not as Mn concentration increases c increases**.** This may suggest that not all Mn ions have replaced Zn in ZnO lattice. Were it so that all Mn atoms replace Zn sites, the Mn substitutions should expand the lattice parameter [18]. The existence of secondary phases (e.g. Mn oxides, Mn clusters or free Mn atoms) is a possible explanation. On the other hand, no odd peaks from the secondary phases were observed in the XRD spectra, possibly due to its detection limitation. In addition, magnetization measurements showed similar behaviors for all Mn doped ZnO films deposited on c-sapphire substrates. The different behavior observed between M-H loops at 300 K (ferromagnetic behavior) and 5 K (superparamagnetic behaviors) may also hint toward the existence of secondary phases which were neither detected by XRD nor SEM.

Defects introduced in the lattice due to Mn doping may be held accountable for the FM behavior. The link between XRD and magnetization measurements is that the thin film deposited at 300 mTorr shows bad quality and the highest M_S which hints toward the relation between the magnetization and the defects. Further investigations are needed to confirm these findings. This may be an explanation of the ferromagnetic loop at 300K, although T_C < 100K. The bad quality of this film may present not only additional phases but also different crystal imperfiction such as line and point defects. TEM analysis is one of the techniques that could compliment this study.

The thin film deposited at 50 and 500 mTorr showed similar ferromagnetic hysteresis and structural properties. These films have nearly the same quality; however, they have different grain sizes. This difference may attribute to the different saturation magnetization between the two films [19].

6 Appendix A: Publications

A paper presenting this work will be published soon. Extended work related to this work has been conducted, the results of which are not presented here as they are still being analyzed. This is mainly due to a shortening of the time limit originally provided for my project. The pending work will be the basis of a second publication as the preliminary results appear to be interesting.

1- "Superposition magnetic behaviors in Mn doped ZnO", S. Venkatesh , A. Baras, I.S. Roqan, will be submitted soon.

2- "The magnetic origin in MnZnO doped with Mg", A. Baras, S. Venkatesh, I.S. Roqan, will be submitted soon.

BIBLIOGRAPHY/REFERENCES

1. Pearton, S.J., et al., *Advances in wide bandgap materials for semiconductor spintronics.* Materials Science and Engineering: R: Reports, 2003. **40**(4): p. 137-168.
2. Wolf, S.A., et al., *Spintronics: A Spin-Based Electronics Vision for the Future.* Science, 2001. **294**(5546): p. 1488-1495.
3. Harish, M., *Application Of Spintronics In Medical Instrumentation*.
4. Pan, F., et al., *Ferromagnetism and possible application in spintronics of transition-metal-doped ZnO films.* Materials Science and Engineering: R: Reports, 2008. **62**(1): p. 1-35.
5. Matsumoto, Y., et al., *Room-Temperature Ferromagnetism in Transparent Transition Metal-Doped Titanium Dioxide.* Science, 2001. **291**(5505): p. 854-856.
6. Dietl, T., et al., *Zener Model Description of Ferromagnetism in Zinc-Blende Magnetic Semiconductors.* Science, 2000. **287**(5455): p. 1019-1022.
7. Zener, C., *Interaction Between the d Shells in the Transition Metals.* Physical Review, 1951. **81**(3): p. 440.
8. Fukumura, T., et al., *Magnetic properties of Mn-doped ZnO.* Applied Physics Letters, 2001. **78**(7): p. 958-960.
9. Jung, S.W., et al., *Ferromagnetic properties of Zn[sub 1 - x]Mn[sub x]O epitaxial thin films.* Applied Physics Letters, 2002. **80**(24): p. 4561-4563.
10. Tiwari, A., et al., *Structural, optical and magnetic properties of diluted magnetic semiconducting Zn1-xMnxO films.* Solid State Communications, 2002. **121**(6-7): p. 371-374.
11. Venkataraj, S., et al., *Structural and magnetic properties of Mn-ion implanted ZnO films.* Journal of Applied Physics, 2007. **102**(1): p. 014905-7.
12. Sharma, P., et al., *Ferromagnetism above room temperature in bulk and transparent thin films of Mn-doped ZnO.* Nat Mater, 2003. **2**(10): p. 673-677.
13. Ozgur, U., et al., *A comprehensive review of ZnO materials and devices.* Journal of Applied Physics, 2005. **98**(4): p. 041301-103.
14. Jagadish, V.A.C.a.C., *Zinc Oxide Bulk: Thin Films and Nanostructures*. First edition ed, ed. C.J.a.S. Pearton: Elsevier.
15. Fan, Z. and J.G. Lu, *Zinc oxide nanostructures: synthesis and properties*. Vol. 5. 2005. 1561-73.
16. Shan, F.K., et al., *Blueshift of near band edge emission in Mg doped ZnO thin films and aging.* Journal of Applied Physics, 2004. **95**(9): p. 4772-4776.
17. Chopra, K.L., S. Major, and D.K. Pandya, *Transparent conductors--A status review.* Thin Solid Films, 1983. **102**(1): p. 1-46.
18. Jun, Z. and et al., *Structure and magnetic properties of Mn-doped ZnO thin films.* Journal of Physics: Condensed Matter, 2007. **19**(3): p. 036210.
19. Diaconu, M., et al., *UV optical properties of ferromagnetic Mn-doped ZnO thin films grown by PLD.* Thin Solid Films, 2005. **486**(1-2): p. 117-121.
20. Karamat, S., et al., *Structural, optical and magnetic properties of (ZnO)1-x(MnO2)x thin films deposited at room temperature.* Applied Surface Science, 2008. **254**(22): p. 7285-7289.
21. Mera, J., et al., *Epitaxial Zn0.9Mn0.1O thin films ablated from targets synthesized by wet chemistry method.* Physica B: Condensed Matter, 2010. **405**(16): p. 3463-3467.

22. Blundell, S., *Magnetism in Condensed Matter*. first edition ed: University of Oxford.
23. Föll, H. *Electronic Materials*. Available from: http://www.tf.uni-kiel.de/matwis/amat/elmat_en/index.html.
24. Graham, B.C.a.C., *Introduction to Magnetic Materials*. second edition ed: WILLY.
25. Reilly, A.; Available from: http://www.physics.wm.edu/~reilly/page3.html.
26. Coey, J.M.D., *Dilute magnetic oxides*. 2009.
27. Hong, N.H., J. Sakai, and V. Brizé, *Observation of ferromagnetism at room temperature in ZnO thin films.* Journal of Physics Condensed Matter, 2007. **19**(3).
28. N. Huong, e.a.
29. Nielsen, K.W., et al., *Ferromagnetism in Mn-doped ZnO due to impurity bands.* Superlattices and Microstructures, 2005. **37**(5): p. 327-332.
30. Venkatesan, M., et al., *Anisotropic Ferromagnetism in Substituted Zinc Oxide.* Physical Review Letters, 2004. **93**(17): p. 177206.
31. Di Trolio, A., et al., *Ferromagnetism above room temperature in Mn-doped ZnO thin films.* Superlattices and Microstructures. **46**(1-2): p. 101-106.
32. Ah Jeon, K., et al., *Magnetic and optical properties of Zn1-xMnxO thin films prepared by pulsed laser deposition.* Journal of Crystal Growth, 2006. **287**(1): p. 66-69.
33. Ueda, K., H. Tabata, and T. Kawai, *Magnetic and electric properties of transition-metal-doped ZnO films.* Applied Physics Letters, 2001. **79**(7): p. 988-990.
34. Schoofs, F., et al., *Strain dependent defect mediated ferromagnetism in Mn-doped and undoped ZnO thin films.* Journal of Applied Physics, 2010. **108**(5): p. 053911-053911-5.
35. Han, Y., *Lecture notes*. 2010.
36. Reimer, L., *Scanning Electron Microscopy Physics of Image Formation and Microanalysis*. Second edition ed. Vol. 45. 1998: Springer.
37. ; Available from: http://academic.brooklyn.cuny.edu/physics/tung/index.htm.
38. Leng, Y., *Materials characterization : introduction to microscopic and spectroscopic methods*. 2008, Singapore; Hoboken, NJ: J. Wiley.
39. Wittke, J.H., *Electron Microscope*. 2006.
40. Ramachandran, T.; Available from: http://www.iitk.ac.in/.
41. QD, *MPMS SQUID VSM User's Manual*. 2007, Quantum Design.
42. HP. Available from: http://hyperphysics.phy-astr.gsu.edu/hbase/solids/squid.html.
43. abyss. Available from: http://abyss.uoregon.edu/~js/glossary/quantum_tunneling.html.
44. Murmu, P.P., et al., *Structural and magnetic properties of low-energy Gd implanted ZnO single crystals.* Nuclear Instruments and Methods in Physics Research Section B: Beam Interactions with Materials and Atoms. **In Press, Corrected Proof**.
45. Larson, B.F. *Introduction to Magnetic Particle Inspection*. 2011; Available from: http://www.ndt-ed.org/EducationResources/CommunityCollege/MagParticle/Physics/Magnetism.htm.
46. *Pulsed Laser Deposition*. 2009; Available from: http://www.itrc.narl.org.tw/Research/Product/Vacuum/pld-e.php.
47. Wongduan Maison, S.A., Tawee Tunkasiri, Prasak Thavornyutikarn and Sukon Phanichphant, *Effect of Calcination Temperature on Phase Transformation and Particle size of Barium Titanate Fine Powders Synthesized by the Catecholate Process.* ScienceAsia, 2001. **27**: p. 239-243.
48. Fukumura, T., et al., *An oxide-diluted magnetic semiconductor: Mn-doped ZnO.* Applied Physics Letters, 1999. **75**(21): p. 3366-3368.

49. Ivill, M., et al., *Magnetization dependence on electron density in epitaxial ZnO thin films codoped with Mn and Sn.* Journal of Applied Physics, 2005. **97**(5): p. 053904-5.
50. Kundaliya, D.C., et al., *On the origin of high-temperature ferromagnetism in the low-temperature-processed Mn-Zn-O system.* Nat Mater, 2004. **3**(10): p. 709-714.
51. Kwang Ho Park, Y.Y.S., Eun Kyung Lee, Lee Seul Son, Suhk Kun Oh, Seong Cho Yu and Hee Jae Kang, *Magnetic and Structural Properties of Mn:ZnO Thin Film Grown on Sapphire(0001) Substrates by using Pulsed Laser Deposition.* Journal of the Korean Physical Society, 2009. **55**(6): p. 2685-2688.
52. Shim, W., et al., *Room-temperature ferromagnetic ordering in Mn-doped ZnO thin films grown by pulsed laser deposition.* Journal of Electronic Materials, 2006. **35**(4): p. 635-640.
53. Veeramuthu Vaithianathan, et al., *Epitaxial Growth of Mn-doped ZnO Thin Films on Al2O3 (0001)* Materials Science Forum, 2004. **449-452**: p. 493-496.
54. Song, C., et al., *Substrate-dependent magnetization in Co-doped ZnO insulating films.* Physical Review B, 2007. **76**(4): p. 045215.
55. Srinivasan, G. and J. Kumar, *Effect of Mn doping on the microstructures and optical properties of sol-gel derived ZnO thin films.* Journal of Crystal Growth, 2008. **310**(7-9): p. 1841-1846.
56. Winter, M. 2010; Available from: http://www.webelements.com/manganese/atom_sizes.html.
57. Lee, G.H., T. Kawazoe, and M. Ohtsu, *Room temperature near-field photoluminescence of zinc-blend and wurtzite ZnO structures.* Applied Surface Science, 2005. **239**(3-4): p. 394-397.
58. Tripathi, S., et al., *Studies of effect of deposition parameters on the ZnO films prepared by PLD.* Nuclear Instruments and Methods in Physics Research Section B: Beam Interactions with Materials and Atoms, 2008. **266**(8): p. 1533-1536.
59. *Magnetic Polarons, Charge Ordering and Stripes.* 2002.
60. *Technical data for Manganese*. Available from: http://periodictable.com/Elements/025/data.html.
61. Pemmaraju, C.D., et al., *Impurity-ion pair induced high-temperature ferromagnetism in Co-doped ZnO.* Physical Review B, 2008. **78**(5): p. 054428.